

NIKHEF Project, Winter Semester 2004-05 : **COACH**

—

Construction Of A Gaseous Cherenkov Detector



performed by:

O. Brandt
S. Cohen
Y. Grange
H. Knuth
M. Takes

supervisor:

P. Kooijman

October 17, 2005

Abstract

*By convention sweet, by convention bitter, by convention hot, by convention cold,
by convention color: but in reality atoms and void.*

Demokrit, V-IV century b.C.

The **COACH** NIKHEF project is the third project organized for all students in the Master Of Particle Physics Program of the UvA. In this project a gaseous Cherenkov detector was simulated, designed, built and operated to measure relativistic charged particles passing through the detector. With this setup the passage of cosmic muons is measured and a spectrum of their energy as a function of the pressure and the composition of the gas is presented.

Contents

1	Introduction	5
2	Theory	7
2.1	Cosmic rays	7
2.1.1	High energy cosmic particles	7
2.1.2	Cosmic air showers	9
2.2	Cherenkov radiation	10
2.2.1	Energy and photon yield	11
2.3	Cherenkov detectors	13
2.3.1	Threshold detectors	13
2.3.2	Differential detectors	13
3	Goals	15
3.1	Educational goal	15
3.2	Technical goal	15
3.3	Scientific goal	15
4	Simulation	17
4.1	Introduction – the need for Monte Carlo	17
4.2	Natural elementary particle flux – a short review	18
4.3	Detector design – fundamental aspects	18
4.3.1	Basic geometric parameters of the experiment	18
4.3.2	Fundamental restrictions for a gaseous Cherenkov detector	20
4.4	Introduction of values reported by the simulation	21
4.4.1	Discussion of errors	23
4.5	The simulation algorithm in detail	26
4.6	Event rates predicted by the simulation	35
5	Setup and Building of the Detector	39
5.1	Detector setup	39
5.1.1	Basic setup and detector quality	39
5.1.2	Mechanical setup	40
5.1.3	The gas system	40
5.1.4	Electronic setup	42
5.2	Components	43
5.2.1	Scintillators	43
5.2.2	Photomultiplier tubes	44
5.2.3	The mirror	45

5.2.4	The window	46
5.3	Estimated detector response	47
6	Measurements and Analysis	49
6.1	Event display	49
6.2	Presentation of the measurements	49
6.3	Data analysis	53
6.3.1	Data analysis using PAW	53
6.3.2	Data analysis using ROOT	57
7	Results and Discussion	59
7.1	Results tables	59
7.2	Graphic presentation of results	59
7.3	Comparison with simulation predictions	62
7.4	Conclusions	63
7.5	Suggestions for future work with the detector	63

Chapter 1

Introduction

This paper is the final report of the Winter Semester 2004-05 NIKHEF Project : **COACH**, a great offering and opportunity for all students in the Masters Of Particle Physics Program of the UvA, who have been **coached** towards a deeper understanding of an extremely fascinating subject – Elementary Particle Physics.

This year's subject to the NIKHEF Project is the construction of a gaseous Cherenkov detector for cosmic radiation, mainly muons. An important goal of this project is to detect cosmic ray muons and measure the spectrum of their energy as a function of the pressure and composition of the gas.

After a brief introduction to cosmic radiation as well as the theory of the Cherenkov effect and detector types based on it, the design of *our* detector and our goals for measurements with it will be presented. We will proceed with a description of its simulation based on Monte Carlo techniques, demonstrate its predictions and discuss their power and quality. Before we present the real measured data and their analysis alongside with our conclusions from these results, an overview over the construction and setting up of the experiment shall be given.

The main intention of this report is to give an introduction to common techniques of experimental and analytical Elementary Particle Physics considering our Cherenkov detector as example as well as to document our work of more than one semester.

We would like to thank our supervisor: Paul Kooijman for his assistance while working on this project and Elisabeth Koffeman and Auke Pieter Colijn for their assistance when Paul was not present. Thanks to Marco Kraan of the NIKHEF engineering department for putting the final design on paper and his advice regarding safety regulations. Also thanks to Edward Berbee and Niels Stoffelen of the mechanical workshop of the NIKHEF for their quick assistance and welding of the pipe.

Chapter 2

Theory

2.1 Cosmic rays

The Earth's atmosphere is constantly bombarded by all kinds of relativistic particles. The cosmic ray particles that enter the terrestrial atmosphere are divided into primary and secondary particles. Primary particles, such as electrons, protons, helium, carbon, iron and other nuclei, are those particles accelerated at astrophysical sources or other nuclei synthesized in stars. Secondary particles are particles produced in the interaction of primaries with the interstellar gas such as lithium, beryllium and boron nuclei.

Cosmic rays were discovered by Victor Hess in 1912. After the discovery of X-rays by Wilhelm Conrad Röntgen in 1895, cosmic rays were seen as radioactive radiation. A survey was done to investigate radioactive substances everywhere; in the crust of the Earth, in the seas, etc. The balloon experiment of Hess showed that the flux actually did not decrease when the altitude of the balloon increased. He concluded that the radiation was not electromagnetic in nature but had its source from out of the cosmos. The cosmic rays became a powerful tool (discovery of the positron) of research in physics and Hess was rewarded for his work with the nobel prize in 1936.

2.1.1 High energy cosmic particles

The energy of the cosmic particles can be enormous. In 1991 the Fly's Eye cosmic ray research group in the USA observed a cosmic ray event with an energy of $3 \cdot 10^{20}$ eV, many orders of magnitude larger than the energy of particles produced in accelerators today. While the composition of the primary particle is not known with certainty, the best guess is that it was a moderate mass nucleus (something like oxygen).

The energy-flux spectrum of cosmic rays is shown in fig. 2.1. After the turnover at $\sim 10^{10}$ eV the spectrum behaves as $\sim E^{-2.7}$ down to the so-called 'knee' at $\sim 3 \cdot 10^{15}$ eV. After the 'knee' it then continues with a steeper slope as $\sim E^{-3.0}$ up to the 'ankle' at $\sim 4 \cdot 10^{18}$ eV. Recent results of the KASCADE array [6] show a substantial difference in the energy spectra of individual types of nuclei around the 'knee'. Today, the change in composition around the 'knee' is considered to be deeply related to a combined influence of acceleration and diffusion of cosmic rays in our galaxy.

From fig. 2.1 it is clear that the cosmic particle flux decreases rapidly from $1 \text{ m}^{-2} \text{ s}^{-1}$ at $\sim 10^{11}$ eV down to $1 \text{ km}^{-2} \text{ yr}^{-1}$ at the 'ankle'. Therefore, detection of higher energy particles is more effective by using a ground array of detectors which makes it possible to sample the

energies from extensive air showers and infer the particle energies indirectly.

The major questions in astro-particle physics are: where are these cosmic ray particles coming from, what are their sources and what kind of mechanisms are responsible for accelerating them to their detected energy. As for the 'low' energy particles ($E < 10^{14}$ eV), their origin and mechanism are fairly well understood. Most of them are protons and electrons ejected from the sun's corona causing the aurora phenomenon in the northern and southern hemisphere.

Cosmic rays with energies $10^{11} < E < 10^{14}$ eV are believed to be mostly due to shock acceleration. In 1949 Enrico Fermi came with an explanation for this acceleration mechanism. According to his theory, protons speed up by bouncing off moving magnetic clouds in space. Exploding stars (supernovae) are believed to act as such cosmic accelerators. Although supernovae are capable of giving these particles their observed energy, they cannot account for the high-energy cosmic rays ($E > 10^{14}$ eV). Cosmic rays in the region $10^{14} < E < 10^{19}$ eV are believed to get their energy from pulsars and galactic winds. The ultra-high energy cosmic-ray particles ($E > 10^{19}$ eV) are believed to be accelerated by enormous electric fields, generated by rapidly spinning, magnetized objects such as neutron stars or active galactic nuclei (AGN).

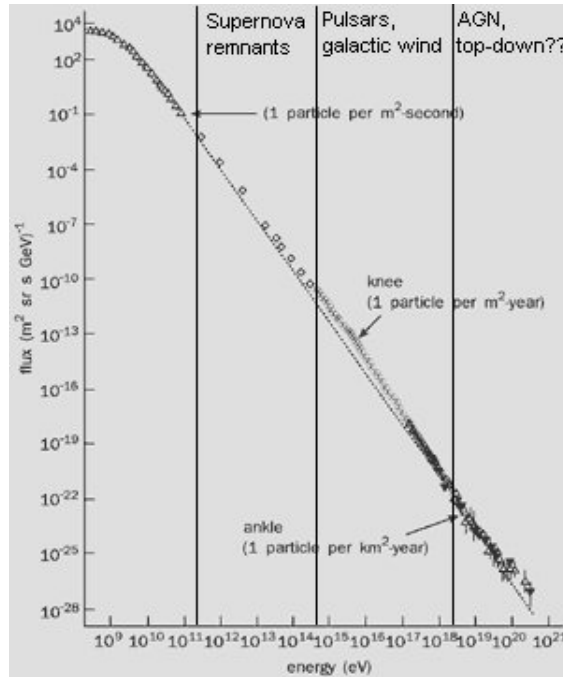


Figure 2.1: The all particle spectrum

GZK cutoff

It was long believed that cosmic ray particles could permeate our surrounding universe. But in 1966 K. Greisen, G. Zatsepin and V. Kuzmin pointed out that high energy cosmic-ray particles ($E > 4 \cdot 10^{19}$ eV) would interact with the cosmic microwave background radiation (CMB). A high-energetic proton for example would interact with a CMB photon according

to the reaction $p\gamma \rightarrow \Delta^+ \rightarrow \pi^0 p$ ending up with a pi zero and a proton. In this process the proton energy and mean free path length would reduce significantly. This energetic discrimination is also known as the GZK-cutoff. It is interesting to look for events above its threshold energy of $4 \cdot 10^{19}$ eV. If such events occur then we know for sure that their source must be local instead of extra-galactic.

2.1.2 Cosmic air showers

When a cosmic ray particle enters the terrestrial atmosphere, it can interact with a nucleus from the atmosphere. If the energy is sufficient a proton will interact with an O_2 or N_2 nucleus. After this first interaction π^0, π^\pm mesons and baryons will be produced. Multiple hadronic interactions follow and the number of particles starts to increase rapidly as this shower or cascade of particles moves downwards in the atmosphere. During their way down particles lose energy and will not be able to create new particles. The shower reaches its maximum when more particles are decaying than being created.

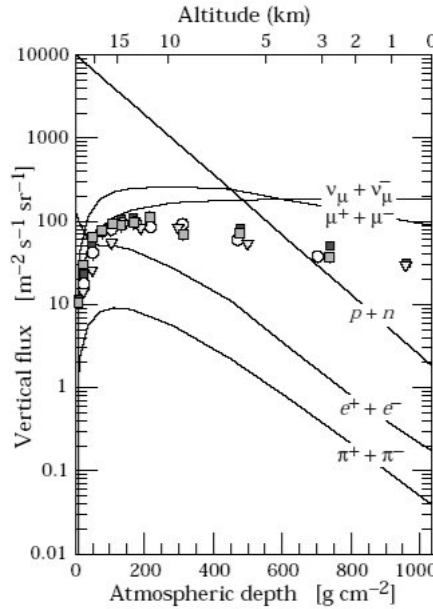


Figure 2.2: Vertical fluxes of cosmic rays in the atmosphere with $E > 1$ GeV. Diagram taken from [1]

When a π^- meson is created it will decay according to $\pi^- \rightarrow \mu^- \nu_\mu$. The muon, which has a mean lifetime of $2.20 \mu s$, will decay into an electron and two neutrinos by $\mu^- \rightarrow e^- \bar{\nu}_e \nu_\mu$. At sea level most of the charged particles are muons, see fig. 2.2. The vertical flux for muons at sea level is $I_{\mu^\pm}(\theta = 0) = 70 \text{ m}^{-2} \text{sr}^{-1} \text{s}^{-1}$ and their mean energy at sea level is $\langle E_\mu \rangle \approx 4 \text{ GeV}$.

To detect the cosmic rays we can use a variety of detectors. Today, much of the collected data about cosmic rays come from fluorescence experiments such as HiRes Fly's Eye and surface detectors such as the AGASA array. AGASA data [4] show an excess of events above the GZK cut-off.

Because of their electromagnetic interaction with matter, detection of secondary relativistic charged particles (e.g. muons and electrons) is possible via detectors such as ionisation,

spark, and cloud chambers. As the particles traverse the atmosphere, detection is also possible due to another phenomenon commonly known as Cherenkov radiation.

2.2 Cherenkov radiation

Cherenkov radiation is a phenomenon widely used in high energy physics. In 1934 Pavel Alekseyevich Cherenkov observed blue light emissions from water irradiated with radioactive particles. He discovered that the particles were travelling at velocities greater than the speed at which light could travel in water. His discovery led to the conclusion that a charged particle will radiate whenever it traverses a dielectric medium with a velocity greater than the local phase velocity of light.

In 1937 Tamm and Frank developed a theory on basis of classical electrodynamics explaining completely all the properties of the new radiation, and predicting new properties and relations. Because of their work P.A. Cherenkov, I.M. Frank and I.Y. Tamm were awarded the nobel prize in October 1958.

The theory of Tamm and Frank is based on an infinite, isotropic and transparent dielectric with $\epsilon \neq 1$ and $\mu = 1$, through which a charged particle is moving along a straight line with a constant velocity v . The Maxwell equations that determine the fields \mathbf{E} and \mathbf{H} are given by

$$\begin{cases} \nabla \times \mathbf{H} = \frac{4\pi}{c} \mathbf{j} + \frac{1}{c} \partial_t \mathbf{D} \\ \nabla \times \mathbf{E} = -\frac{1}{c} \partial_t \mathbf{H} \\ \nabla \cdot \mathbf{H} = 0 \\ \nabla \cdot \mathbf{D} = 4\pi\rho \end{cases}$$

Eventually the equations yield a general solution of two Hankel functions of first and second kind; H_0^1 and H_0^2 . At small velocities, i.e. $\beta n < 1$, the particle does not radiate. However a completely different result is obtained if $\beta n > 1$. The two Hankel functions then represent a cylindrical wave. The resulting vector potential \mathbf{A} is given by

$$A_z = - \int_{-\infty}^{+\infty} d\omega \frac{ie}{c\sqrt{2\pi s\xi}} e^{i\omega(t - \frac{z \cos \theta + s \sin \theta}{n(\omega)}) + \frac{\pi}{4}i}; \quad A_s = 0; \quad A_\phi = 0 \quad (2.1)$$

with s, ϕ and z cylindrical coordinates, θ the angle between the propagation vector and the z-axis, c and $n(\omega)$ respectively the velocity of light and index of refraction, e the particle charge (in esu), ξ a solution parameter and ω the frequency of the wave.

The integral in 2.1 is in fact a sum of conical waves of frequency ω propagating at an angle θ to the axis z , which coincides with the motion of the particle (see figure 2.3).

It follows from eq. 2.1 that the particle will only radiate when $\beta n > 1$. The radiation then propagates at an angle θ to the direction of the particle's motion. From figure 2.3 it is easy to see that this angle is related to the particle's velocity $\beta = \frac{v}{c}$ via the simple expression

$$\cos \theta(\omega) = \frac{ct}{n(\omega)} \frac{1}{vt} = \frac{1}{n(\omega)\beta} \quad (2.2)$$

Also from eq. 2.2 it is clear that the threshold velocity is given by $\beta_{\text{thresh}}n(\omega) = 1$ which corresponds to an opening angle $\theta = 0$. Whenever $\beta < \beta_{\text{thresh}}$, Cherenkov radiation will not occur and eq. 2.2 is not defined.

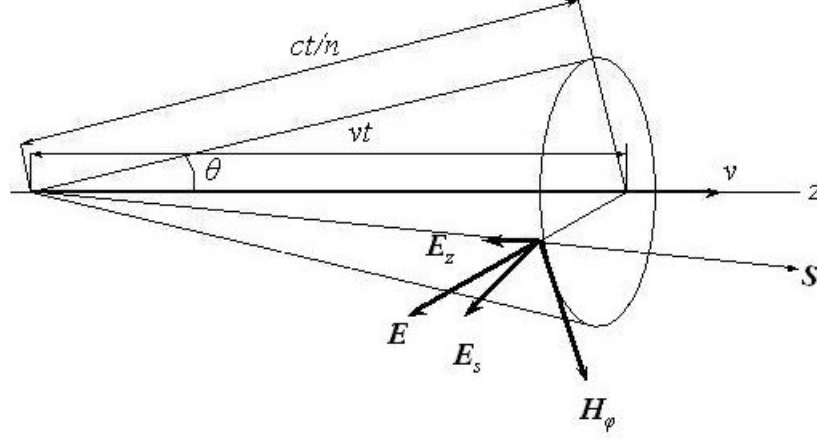


Figure 2.3: The mutual orientation of the vectors \mathbf{E} , \mathbf{H} and \mathbf{S} for the Cherenkov radiation cone described by the theory of Tamm and Frank. Here \mathbf{S} is the Poynting vector, $\frac{c}{n(\omega)}$ the velocity of light in the medium, θ the Cherenkov opening angle and v the velocity of the particle.

In 1940 V.L. Ginzburg came with a quantum mechanical treatment of the Cherenkov effect by solving the Dirac equation of a spin 1/2 particle interacting with a photon field. He derived that the emitted photon possesses two polarization states, one parallel and one perpendicular to the plane defined by the initial momentum of the particle and the momentum of the emitted photon, congruent with fig. 2.3.

2.2.1 Energy and photon yield

Both Tamm and Frank as well as Ginzburg were able to calculate the amount of energy emitted per unit path length per unit frequency by a particle with charge Ze . The relation that Ginzburg found is given by

$$\frac{d^2E}{dx d\omega} = -\frac{v_{ph}}{v_{gr}} \frac{Z^2 \alpha \hbar}{c} \left(1 - \frac{1}{n(\omega)^2 \beta^2} \right) \omega \quad (2.3)$$

with the fine structure constant $\alpha = \frac{e^2}{\hbar c}$, and $v_{ph} = \frac{\omega}{k}$ and $v_{gr} = \frac{d\omega}{dk}$ respectively the phase and group velocity of light. If the refractive index of the medium is independent of the frequency¹, then $v_{ph} = v_{gr}$ and eq. 2.3 will be equivalent to the relation Tamm and Frank derived. Using the relation $\omega = \frac{2\pi c}{\lambda}$ and the assumption above we can rewrite eq. 2.3 in terms of the radiation's wavelength

$$\frac{d^2E}{dx d\lambda} = \frac{4\pi^2 Z^2 \alpha \hbar c}{\lambda^3} \left(1 - \frac{1}{n(\lambda)^2 \beta^2} \right) \quad (2.4)$$

¹The group velocity is given by $v_{gr} = v_{ph} \left(1 - \frac{k}{n} \frac{dn}{dk} \right)$. If the index of refraction of the medium is independent of the frequency, i.e. $\frac{dn}{dk} = 0$, then $v_{ph} = v_{gr}$.

Because the energy of a photon is related to its frequency by $E = \hbar\omega = \frac{2\pi\hbar c}{\lambda}$, we can rewrite eq. 2.4 to get the Cherenkov photon yield in terms of the number of photons emitted per unit path length and per unit wavelength

$$\frac{d^2 N}{dx d\lambda} = \frac{2\pi Z^2 \alpha}{\lambda^2} \left(1 - \frac{1}{n(\lambda)^2 \beta^2} \right) \quad (2.5)$$

Integration of eq. 2.4 and eq. 2.5 over dx explains the blue light observation Cherenkov made. Because $\frac{dE}{d\lambda} \propto \frac{1}{\lambda^3}$ and $\frac{dN}{d\lambda} \propto \frac{1}{\lambda^2}$ photon emission will be predominantly in the ultra-violet part of the spectrum (see fig. 2.4).

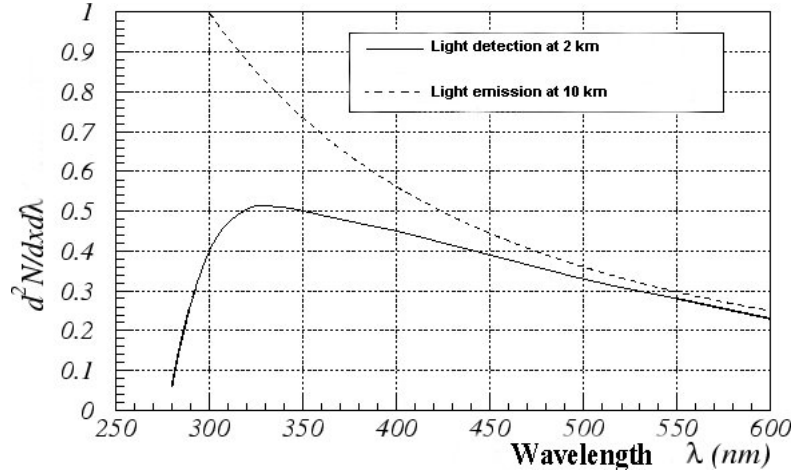


Figure 2.4: Differential Cherenkov photon spectrum within the atmosphere. Light emission at 10 km is given by the dashed line. Light collection given by the continuous line includes absorption by ozone and Rayleigh and Mie scattering.

To get the total energy per unit pathlength we need to integrate eq. 2.4 over $d\lambda$ which gives us

$$\frac{dE}{dx} = 4\pi^2 Z^2 \alpha \hbar c \int_{\beta > \beta_{\text{thresh}}} d\lambda \left(1 - \frac{1}{n(\lambda)^2 \beta^2} \right) \frac{1}{\lambda^3} \quad (2.6)$$

and the the total number of photons per unit path length is

$$\frac{dN}{dx} = 2\pi Z^2 \alpha \int_{\beta > \beta_{\text{thresh}}} d\lambda \left(1 - \frac{1}{n(\lambda)^2 \beta^2} \right) \frac{1}{\lambda^2} \quad (2.7)$$

In practice, the index of refraction $n(\lambda)$ is fairly constant over the region of interest $[\lambda_1, \lambda_2]$. Finally, integration from λ_1 to λ_2 gives us the interesting relations

$$\frac{dE}{dx} = 4\pi^2 Z^2 \alpha \hbar c \left(1 - \frac{1}{n(\lambda)^2 \beta^2} \right) \left(\frac{1}{\lambda_1^2} - \frac{1}{\lambda_2^2} \right) \quad (2.8)$$

$$\frac{dN}{dx} = 2\pi Z^2 \alpha \left(1 - \frac{1}{n(\lambda)^2 \beta^2} \right) \left(\frac{1}{\lambda_1} - \frac{1}{\lambda_2} \right) \quad (2.9)$$

A detailed discussion about Cherenkov radiation can be found in Zrelov's book [5].

Pressure

While the index of refraction is fairly constant over a wavelength region $[\lambda_1, \lambda_2]$, it does vary significantly when we change the pressure of the gas. The index of refraction therefore depends more on the pressure than on the wavelength of the light, so we can rewrite 2.2 as

$$\cos \theta(P) = \frac{1}{n(P)\beta} \quad (2.10)$$

where

$$n(P) = 1 + (n_0 - 1) \frac{P}{P_0} \quad (2.11)$$

with n_0 the index of refraction at 1 atm.

2.3 Cherenkov detectors

Cherenkov detectors can be divided into three types; (1) threshold detectors, (2) differential detectors and (3) ring imaging detectors (RICH or CRID). In this paragraph we will not discuss the latter.

In general Cherenkov detectors must contain two main elements: (1) a radiator (e.g. water or gas) through which a charged particle passes thereby making Cherenkov emission possible and (2) a photodetector also known as a photo multiplier unit (PMT). The choice of the radiator depends on the velocity spectrum of the particles that would be detected and the desired radiation length. Accordingly the refractive index and the absorption length of the radiator are chosen. In any case it is preferable that the radiator is highly transparent in the UV-part of the spectrum to guarantee a high detection efficiency of the Cherenkov light.

2.3.1 Threshold detectors

Threshold detectors are only able to detect the presence of emitted Cherenkov light. In general they have a fairly simple design (see fig. 2.5).

Threshold detectors only give a signal when the particle's velocity (usually of π 's, K 's or p 's) is above a certain threshold velocity i.e. $\beta > \beta_{\text{thresh}}$. Therefore they only provide information on how many particles are present above a certain velocity β in a given time window. This threshold velocity depends, of course, on the index of refraction n of the radiator via $\beta_{\text{thresh}}n = 1$. Above the threshold velocity the Cherenkov opening angle is given by equation 2.2. Table 2.1 reports on commonly used radiator materials, their refractive index and their momentum thresholds for different particles. It can be seen that by combining three threshold detectors using these three radiators, if the momentum of a particle is known, its type could be uniquely determined for several momentum ranges simply by looking for signal/no signal in the three detectors. So, threshold detectors can be used for particle identification.

2.3.2 Differential detectors

Differential Cherenkov detectors (see fig. 2.6) only give a signal for particles within a certain range of β . They use optical focusing and/or geometrical masking to select particles emitting

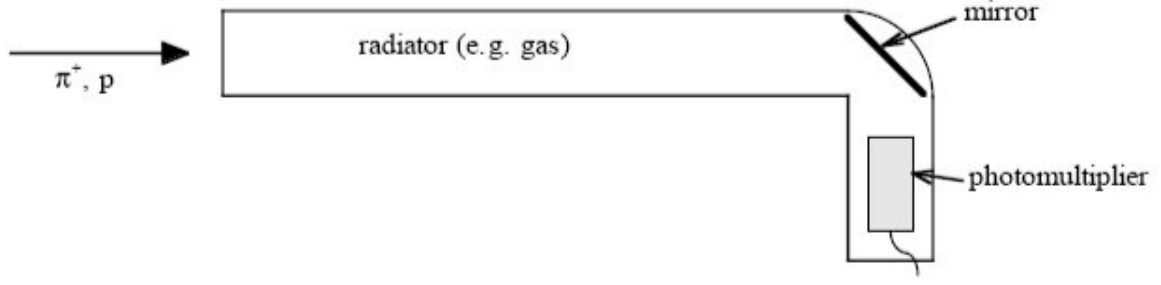


Figure 2.5: Basic design of a threshold Cherenkov detector.

	Refractive index	$p_{th}(\text{GeV})$	$p_{th}(\text{GeV})$	$p_{th}(\text{GeV})$
Material	n	π	K	p
Aerogel	1.024	0.6	2.2	4.2
Freon 114	1.0014	2.7	9.4	17.8
CO ₂	1.00043	4.8	16.9	32.0

Table 2.1: Radiators used in Cherenkov detectors and their refractive index and momentum thresholds for different particles.

Cherenkov radiation in a certain range of opening angle $\theta \pm \Delta\theta$ and thus specify a certain velocity interval. A velocity resolution of $\frac{\sigma_\beta}{\beta} \sim 10^{-5}$ can be obtained.

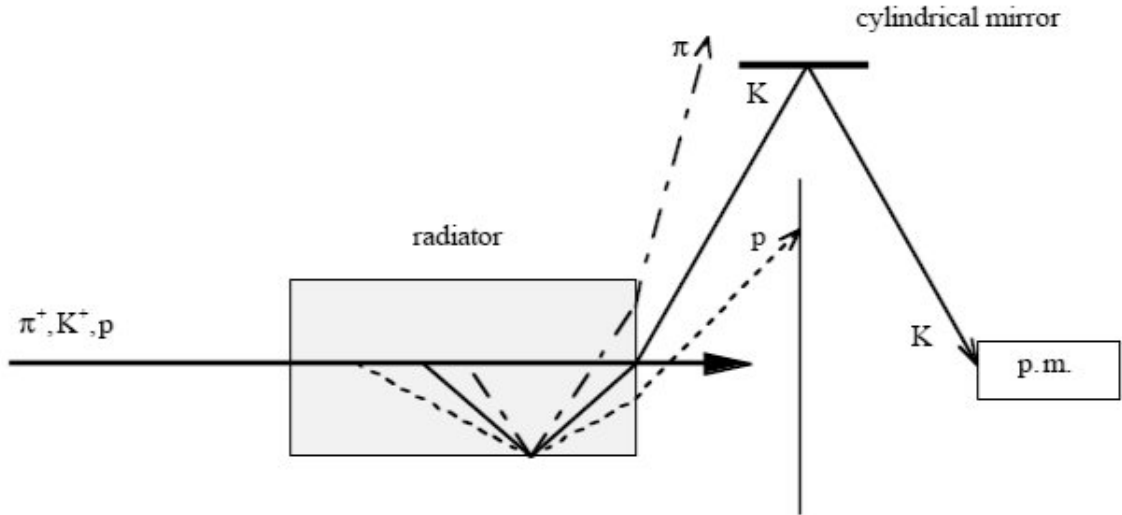


Figure 2.6: Basic design of a differential Cherenkov detector.

Chapter 3

Goals

The COACH project has actually three goals. The project covers both the technical aspect of building a working Cherenkov detector and the scientific aspect of analysing the collected data. The educational aspect of achieving those goals can be seen as the main purpose of the project.

3.1 Educational goal

The most important goal of the COACH project is the educational goal. It can be best described as *"to learn how to invent and build a new experiment with a group and run it"*. The first part of this goal is somewhat twofold because it contains the collaboration between the members of the group as individuals as well as with the people of the workshop, who actually assemble and build the different components of the detector. The second part of this goal has to do with creating and validating raw data so it could be analysed.

3.2 Technical goal

A concise description of the technical goal is the title of the project itself *"the construction of a gaseous Cherenkov detector"*. This goal cannot be reached without the mechanical workshop. Our part in this goal is actually to make the plans for the construction and to deliberate about those plans with the workshop and later to assemble the detector from the components produced by the workshop. Another technical part of the project is creating a simulation of the detector and obtaining results with it, which can be compared to our experimental results.

3.3 Scientific goal

The third important goal of this project is the scientific goal: *"detecting muons and measuring a spectrum of their energy as a function of pressure and composition of the gas"*. This means the acquisition of raw data with the Cherenkov detector and the analysis of this data with software packages as ROOT ¹ and PAW ². Eventually a comparison between the simulated and acquired data is made and results and conclusions are obtained.

¹ROOT, an object oriented data analysis framework, see <http://root.cern.ch>

²PAW: Physics Analysis Workstation, see <http://wwwasd.web.cern.ch/wwwasd/paw/>

Chapter 4

Simulation

The very first questions a physicist asks him/herself when thinking of an experiment or designing it, are: "What exactly will I be able to measure with such a setup? What results do I expect?" The next questions, after performing the experiment, are: "Do the measurements fit my expectations respecting the measurement uncertainties? How can a significant deviation be explained?"

In this chapter we will try to answer the first two questions applied to the special case of our detector and to lay a basis for approaching the last ones, which will be the subject of chapter 7: RESULTS on page 59.

4.1 Introduction – the need for Monte Carlo

Since we build a gaseous CO₂ Cherenkov detector with a maximum working pressure of $P_{\max} = 5 \text{ atm}$ (this maximum pressure was chosen for safety reasons, the security valve was set to 6 atm), the maximum Cherenkov cone opening angle θ_{emiss} is limited to

$$\theta_{\text{emiss}}^{\max} = \arccos \frac{1}{\beta n} \Big|_{\beta=\beta_{\max} \equiv 1, n=n(P=5\text{atm})=1.00205} \simeq 3.67. \quad (4.1)$$

Considering this fact we realize that this value is too small for us to be able to build a differential Cherenkov detector in order to register each momentum region separately (for details see section 2.3.2). Thus, the only information we can get from a single event is the fact that we have detected a charged particle with a certain β_{particle} exceeding the threshold for Cherenkov radiation $\beta_{\text{particle}} > \beta_{\text{thresh}}(P)$, where $\beta_{\text{thresh}}(P)$ follows from the Cherenkov condition:

$$\frac{1}{\beta_{\text{thresh}} n(P)} \stackrel{!}{=} \cos \theta \Big|_{\theta=\theta_{\min} \equiv 0} \equiv 1 \quad \Rightarrow \quad \beta_{\text{thresh}} = \frac{1}{n(P)}. \quad (4.2)$$

We see that we cannot draw a serious scientific conclusion on an event-by-event basis. If we want to measure the elementary particle flux $\Phi := \frac{dN}{dS dt}$ in e.g. $[\text{s}^{-1} \text{m}^{-2}]$ or intensity $I := \frac{dN}{dS dt d\Omega}$ in $[\text{s}^{-1} \text{m}^{-2} \text{ster}^{-1}]$ via a measurement of a *passage rate* \dot{N} in $[\text{s}^{-1}]$:

$$\dot{N} := \frac{dN}{dt} = \int dS \Phi = \int dS d\Omega I$$

of elementary particles through our detector, we have to take a statistical approach. It can be done by means of a simulation in the following way: first the particles are generated

according to the theoretical prediction (in our case empirical data reported in [1, 2], which will be the subject of the next section) considering the intensity I , its composition, momentum and angular distribution; in the second step the response of our detector to it is simulated. This is done on an event-by-event basis and takes into account experimental parameters like dimensions, the kind of gas filled, its pressure P etc. At the end of this procedure stands a prediction about the expected number of events N per unit time, or an EVENT RATE \dot{N} in $[s^{-1}]$. This we can do for different pressures P , which will give us an idea about elementary particle fluxes with β -values above the corresponding threshold $\beta_{\text{thresh}}(P)$. Finally, these numbers can be compared with actual measured values. This will be done in chapter 7. If one did the job right, the predicted and measured values correspond respecting the errors. If this is not the case, either the simulation does not describe the experiment properly, a mistake was made when performing the experiment or one has discovered new physics. This approach, quite often used in Particle Physics, is called MONTE CARLO method. Indeed it is the only way to give a satisfying answer to the first two questions raised in the first paragraph of this chapter.

4.2 Natural elementary particle flux – a short review

Since we do not have any accelerator available, our goal is to measure the natural elementary particle flux. Leaving a discussion about its origin and creation mechanisms aside, it consists according to the values reported in [2] mainly of muons, electrons and hadrons (and their antiparticles) in a rough proportion of 70:30:1. Since the electrons are rather low-energetic due to their origin in electromagnetic cascades and offer little relevant directional information about the primary point of the cascade, our goal is a measurement of the atmospheric muon intensity. Thus, we will have to relate our measurements to the value of $I_{\mu^\pm}(\theta = 0) = 70 \text{ m}^{-2} \text{ ster}^{-1} \text{ s}^{-1}$ with a trend towards lower normalization by 10-15% for muons with a momentum $p_\mu > 1 \text{ GeV}$, as reported in [2].)

4.3 Detector design – fundamental aspects

The principal design of our detector is already determined by the requirements of measuring the cosmic muon flux and intensity for different gas pressures. However, an optimal design is searched for by means of a Monte Carlo method. This approach is very common in Astroparticle/Particle Physics and implies that the simulation has to be set up first and that the simulated detector geometry and parameters are varied in the simulation.

4.3.1 Basic geometric parameters of the experiment

Dimensions

To begin our search for the detector optimal dimensions, let us consider the formula for Cherenkov photon yield

$$\frac{d^2 N}{dx d\lambda} = \frac{2\pi\alpha}{\lambda^2} \left(1 - \frac{1}{\beta^2 n^2} \right). \quad (4.3)$$

where we have taken Z in eq. 2.5 equal to one. Clearly, $\frac{dN}{d\lambda}$ is linear in x , which means that an ideal detector should be infinitely long. Of course, it is absolutely unrealistic in terms of realization. But there is also another problem limiting the length l implicitly: the Cherenkov

opening angle θ_{emiss} is finite and given by eq. 4.1 for the ideal case ($P = 5 \text{ atm}$). It implies that the photons will be spread over a larger area at the detector bottom (limited by detector tube cross section S) with increasing detector length l . The square root of the detector cross section area over its length should not be significantly smaller than the emission angle in radian:

$$\frac{\sqrt{S}}{l} \stackrel{!}{>} \theta_{\text{emiss}}^{\text{max}} [\text{rad}].$$

Yet, there is another aspect to it – a larger detector tube cross section spans a larger solid angle Ω , therefore the flux and the event rate will be larger: $\dot{N} = \int dS \Phi = \int dS d\Omega I$. Considering all this and two more practical limitations: the finite ceiling height and a limited detector volume (gas costs & detector weight), we have chosen an aluminum tube with a length of $l = 2 \text{ m}$ and an inner radius $R = 13.5 \text{ cm}$, which was stored at the NIKHEF workshop.

Orientation

From the previous chapter we know what we are going to measure – namely the natural intensity of atmospheric muons. Since by far the largest part of muons originates from decays of products of hadronic interactions of cosmic protons with the atmosphere molecules, featuring a decay length roughly given by the height of the primary interaction point from ground, the shape of the angular intensity distribution is proportional to a cosine squared: $I \propto \cos^2 \theta$, where θ is the ascension angle in cylindrical coordinates. Thus, to obtain the highest possible event rate \dot{N} , the following relationship should hold:

$$\theta \stackrel{!}{=} 0,$$

or in other words, our detector should be oriented orthogonal to the Earth surface.

Mirror and detecting system

So far we have discussed the detector body only. Now a question arises: how to detect Cherenkov radiation in the most convenient way? We decided for a PMT (PHOTO MULTIPLIER TUBE) with an active photocathode diameter of 12.5 cm. However, just putting it at the bottom of the detector is not the best option – a large fraction of Cherenkov radiation will simply miss it on the one hand and the muons traversing it can likely induce a correlated signal by depositing some ionization on the other hand. These are strong arguments to place the PMT in a short 90°-sidearm of the same cross sectional dimensions as the detector body and to install a 45°-mirror to reflect the photons onto it. We are using a nickelled parabolic mirror (made of a satellite dish, for details we refer to chapter 5), which focuses the radiation at the same time. Because of the overpressure inside of the detector body the PMT is placed outside of it looking through a window. Regular glass window was found to be not very much transperant to the Cherenkov light UV wavelengths, thus not usable for us, and so we chose to use a more expensive but highly translucent borosilicate glass window. All the mentioned geometrical features are fully simulated, for details refer to section 4.5. You can get an idea of how our detector looks like from fig. 4.2 on page 28.

4.3.2 Fundamental restrictions for a gaseous Cherenkov detector

The third aspect we needed to think about before making a reasonable design proposal was the low photon yield of any Cherenkov emission process, especially with a gaseous emission medium featuring a rather low n , compared to a scintillator for example. Let us compare the two values:

- a typical plastic scintillator like the one we are using in our coincidence unit (see bottom of the current section 4.3.2) of 0.5 cm thickness gives us on average $\sim 10^4$ photons per passage of one MIP (MINIMUM IONIZING PARTICLE, see [1] for its definition) with a typical energy deposit per path length of $\langle -\frac{dE}{dx} \rangle \cong 1.8 \text{ MeV cm}^{-1}$.
- To determine the photon yield of our detector let us assume:
 - a charged particle traverses its full length l ;
 - the wavelength interval "available" for Cherenkov photon emission is [300, 600] nm, the lower boundary imposed by increasing opaqueness of CO_2 in ultraviolet range, the upper one by insensitivity of a typical PMT in red and infrared range of the spectrum;
 - the minimum pressure to work with: $P \doteq 1 \text{ atm}$, thus $n = n_{\text{CO}_2} = 1.00041$;
 - $\beta \doteq 1$.

With these assumptions the integration of the differential photon yield eq. 4.3 gives:

$$\begin{aligned}
 N &= \int dx d\lambda \left. \frac{d^2 N}{dx d\lambda} \right|_{\beta=1, n=n_{\text{CO}_2}} \\
 &= 2\pi\alpha \cdot l \cdot \left(1 - \frac{1}{\beta^2 n^2} \right) \Big|_{\beta=1, n=n_{\text{CO}_2}} \cdot \left[-\frac{1}{\lambda} \right]_{300\text{nm}}^{600\text{nm}} \\
 &\simeq 125,
 \end{aligned}$$

which corresponds to $\frac{dN}{dx} = 0.63 \text{ cm}^{-1}$.

Clearly, $10^4 \gg 125$; but in order to realize how difficult the situation really is with Cherenkov detectors compared to conventional ones we shall remember the fact that the input conditions stated for our estimation above are for the optimal case (except for $P = 1 \text{ atm}$). We have considered $\beta \equiv 1$, but due to the $1 - 1/(\beta^2 n^2)$ term even a tiny deviation of β from 1 plays a crucial role. It means that in the worst case, i.e. for a muon with a momentum just above the detection threshold: $p_\mu - p_{\text{thresh}} \ll p_{\text{thresh}}$ we will get a much smaller number of emitted photons, typically $\mathcal{O}(10)$. In order to know how strong a certain p_{thresh} affects the detectable fraction of the natural muon spectrum let us calculate it. Our starting point is the threshold condition 4.2:

$$\frac{1}{\beta_{\text{thresh}} n} \stackrel{!}{=} \cos \theta \Big|_{\theta=\theta_{\min} \equiv 0} \equiv 1 \quad \Rightarrow \quad \beta_{\text{thresh}} = \frac{1}{n} = 0.99959 \text{ (!)}$$

with this value we obtain:

$$\begin{aligned}
 p_{\text{thresh}} &= \beta \gamma \cdot m_\mu \Big|_{\beta=\beta_{\text{thresh}}} && \text{with } \gamma := \frac{1}{\sqrt{1 - \beta^2}} \\
 &= 3.69 \text{ GeV}
 \end{aligned}$$

Clearly, $p_{\text{thresh}} = 3.69 \text{ GeV}$ is a rather unpleasant message, since from the last section we know that the mean value of the flux ($\frac{d\Phi}{dp}(p_{\text{max}}) = \langle \frac{d\Phi}{dp} \rangle$) lies approximately at $p_{\text{max}} = 4 \text{ GeV}$. In other words, at $P = 1 \text{ atm}$ we will miss quite exactly half of the total energy flux, which also means due to the exponential drop of the flux distribution: $\frac{d\Phi}{dp}(p) \propto e^{-2.7p}$, we will miss much more than half of the particles flux.

Finally we must take into account that for both detection methods we have not yet considered the limited Q.E. (QUANTUM EFFICIENCY) of the PMT, typically $\langle \text{Q.E.} \rangle \simeq 0.15$, and $\text{Q.E.}_{\text{peak}} < 0.3$, which worsens the signal amplitude and its statistics even more, not to speak about the fraction of Cherenkov photons to *arrive* at the PMT window.

The need for a coincidence unit

Regarding the considerations above, we realize that for a large fraction of muon passage events the number of Cherenkov photons to eventually hit the PMT cathode will be 1 or slightly larger. It is evident that under normal condition these events will not be discriminable from noise. Thus, we need an additional coincidence unit to give us a gate for the signal in the order of 20-50 ns. Such a time gate is fully sufficient as it surely covers the maximum propagation time of both the muon and the photons in the 2m long detector.

How do we realize now a coincidence unit? If we lived in an ideal world and were not limited by our budget, we would put 2 round scintillators, exactly the size of the detector tube cross section at its top and bottom. Unfortunately this is not the case, so we had to get by with what was available: a quadratic scintillator of $31 \times 31 \text{ cm}$ and two rectangular ones of $31 \times 50 \text{ cm}$. Thus, we have positioned the quadratic scintillator in 25 cm distance *above* the top of the detector tube parallel to the Earth surface, and the two rectangular ones also in 25 cm distance *below* its bottom, in such a way, that the area of their overlap is $31 \times 31 \text{ cm}$. We have built a special metal rack to support the coincidence system. You can get an idea how the whole setup looks like from fig. 4.2 on page 28. Finally, we connected the outputs of all the 3 scintillators to a coincidence unit.

4.4 Introduction of values reported by the simulation

Now, after a brief introduction to the experiment and methodology needed for a serious scientific analysis let us introduce some values to be reported by the simulation, their experimental accessibility and, in the second part of this section, their predictive power, i.e. statistical and systematic uncertainties.

Event numbers

The most basic value to be an input to a simulation is the so-called EVENT NUMBER N_{event} , which in our case instructs the simulation how many incident muons with a momentum high enough to emit Cherenkov radiation and to pass through the scintillator coincidence unit have to be generated. This number *alone* is of no relevance, but if you compare it with the *total* number of muons with $p_{\mu} > 1 \text{ GeV}$: N_{μ}^{incid} (i.e. including the ones which do not fulfill the Cherenkov condition 4.2), you can get an idea about what fraction of the spectral range $[1, \infty) \text{ GeV}$ you in principle can measure (in our simulation ∞ is approximated by 300 GeV , which is fairly good enough due to the exponential drop of the momentum distribution of atmospheric muons: $dN/dp \propto e^{-2.7p}$). And if you relate N_{event} to the *registered* event number N_{μ}^{rgstd} , you will learn about the efficiency of your detector.

One other interesting value accessible via event numbers is the INTEGRATED FLUX RATIO for *different* momentum thresholds, which can be compared to integrated fluxes:

$$\frac{N_1(p_\mu > p_{\text{thresh}_1}(P_1))}{N_2(p_\mu > p_{\text{thresh}_2}(P_2))} \cong \frac{\Phi_1(p_\mu > p_{\text{thresh}_1}(P_1))}{\Phi_2(p_\mu > p_{\text{thresh}_2}(P_2))},$$

as reported in [2] or [3]. So, what we can do is to compare simulated (and, of course, experimental) event numbers for different pressures P , and therefore different momentum thresholds $p_{\text{thresh}}(P)$. However, this value will not have a large predictive power, since with an altering P not only the threshold varies, but also the detector efficiency over the *whole* momentum range. Thus we will measure the integration of the flux distribution multiplied by the efficiency function, a rather abstract value.

Please notice that in the following discussion we will refer to *all* the introduced N_{\dots} numbers as event numbers.

Time passed in the experiment

Before we can transfer the three event numbers mentioned above to corresponding event rates, we need to introduce an important concept: the so-called TIME PASSED IN THE EXPERIMENT t_{passed} . The need for it is clear: our simulation generates a certain number of muons traversing our detector, which has to be related to the time, that would *on average* have passed in a real experiment: t_{passed} (note that we omit the $\langle \cdot \rangle$ -notation for t_{passed}). How do we obtain it? As discussed in the previous section, we must relate it to the reference empirical intensity of cosmic muons with a momentum $p_\mu > 1 \text{ GeV}$: $I_{\mu^\pm}(\theta = 0, p_\mu > 1 \text{ GeV}) = 70 \text{ m}^{-2} \text{ ster}^{-1} \text{ s}^{-1}$, as reported in [2], which predicts a certain mean event rate

$$\begin{aligned} \langle \dot{N}_{1 \text{ GeV}} \rangle &= \int dS d\Omega I \\ &= S \cdot \int d\Omega I \quad \text{with } S = 31 \text{ cm} \times 31 \text{ cm} \\ &\cong S \cdot \Omega \cdot I \quad \text{with } \Omega = \frac{31 \cdot 31 \text{ cm}^2}{200^2 \text{ cm}^2} \\ &= 0.103 \text{ s}^{-1} \end{aligned} \tag{4.4}$$

for incident muons passing through the scintillator coincidence unit. Note that in the last but one step we have used that $I(\theta) \cong I_0 \cdot \cos^2 \theta = I_0 \cdot (1 - \mathcal{O}(\theta^2))$, leading to an error of $\mathcal{O}(\theta^3)$ ($< 10^{-3}$) after integration, which is reasonable value for small θ , which is true in our case: $\theta < 0.088 \text{ rad}$.

Now we can determine the mean time between two events:

$$\langle T_{1 \text{ GeV}} \rangle = \frac{1}{\langle \dot{N}_{1 \text{ GeV}} \rangle} = 9.67 \text{ s}.$$

Finally, the t_{passed} can be calculated:

$$t_{\text{passed}} = N_\mu^{\text{incid}} \cdot \langle T_{1 \text{ GeV}} \rangle. \tag{4.5}$$

Please remember that in our notation $N_\mu^{\text{incid}} \equiv N_{1 \text{ GeV}}$.

Event rates

Now we are fully equipped for a discussion of EVENT RATES. In general a rate can be defined as $\dot{N}_{\dots} := N_{\dots} / t_{\text{passed}}$. We should keep in mind that in our case it is an *average* value, though again we omit the $\langle \cdot \rangle$ -notation. In such a way we can calculate the rate of muons with a momentum above 1 GeV: $\dot{N}_{\mu}^{\text{incid}}$ (which is by definition just $1/\langle T_{1\text{ GeV}} \rangle$), the rate of muons emitting Cherenkov radiation \dot{N}_{event} (however, it is not implemented in the simulation program since the value it predicts is experimentally not accessible), the registered muon rate $\dot{N}_{\mu}^{\text{rgstd}}$ and the total $(p^{\pm} + \mu^{\pm} + e^{\pm})$ rate \dot{N}_{total} . The latter can be calculated from the basic proportions $I_{\mu^{\pm}} : I_{e^{\pm}} : I_{p^{\pm}} = 70 : 30 : 1$ (as given in [1]) according to the formula:

$$\dot{N}_{\text{total}} = \left(1.38 + \frac{I_{e^{\pm}} + I_{p^{\pm}}}{I_{\mu^{\pm}}} \right) \cdot \dot{N}_{\mu}^{\text{incid}} = 1.82 \dot{N}_{\mu}^{\text{incid}} = 1.88 \text{ s}^{-1}, \quad (4.6)$$

where the $1.38 \dot{N}_{\mu}^{\text{incid}}$ -term represents the total natural muon spectrum with $p_{\mu} \in [0.1, 300] \text{ GeV}$, since $I_{\text{total}}^{\mu} / I_{1\text{ GeV}}^{\mu} \simeq 1.38$ according to [3].

At the end, let us give the explicit formula for most important reported value, the rate of registered muons $\dot{N}_{\mu}^{\text{rgstd}}$ once again:

$$\dot{N}_{\mu}^{\text{rgstd}} = \frac{N_{\mu}^{\text{rgstd}}}{t_{\text{passed}}}. \quad (4.7)$$

4.4.1 Discussion of errors

Before the software implementation and the results from the simulation are discussed in the last two sections, let us briefly discuss the statistical and systematic uncertainties ("errors") to the values predicted by the simulation.

Event numbers: error discussion

In principle, N_{event} is free of *statistical* errors, as it is an input to the simulation program. But what about the two other event numbers, in the first place N_{μ}^{rgstd} ? A proper discussion of this issue is very difficult and a satisfying answer for all pressures cannot be given. The reason is the following: surely we can estimate the mean value of registered muons, it is N_{μ}^{rgstd} itself, no matter which shape the PDF (PROBABILITY DISTRIBUTION FUNCTION) has. But in order to determine a statistical uncertainty of this predicted value the shape of the PDF must be known, which will be rather a subject to a Masters of Theoretical Physics or Numerical Calculus than to the NIKHEF project. You can get an idea about the complexity of this problem by taking a glance at figure 4.1. It shows two scatterplots: the number of emitted photons N_{γ}^{emit} and the registered ones $N_{\gamma}^{\text{rgstd}}$ versus muon momentum p_{μ} for $P = 3 \text{ atm}$. All the points in the right plot, for which $N_{\gamma}^{\text{rgstd}}$ is 0 represent not registered muons, although they fulfill the Cherenkov condition. Of course, this happens more likely for p_{μ} just above threshold with low numbers of emitted photons N_{γ}^{emit} , but not exclusively, as a muon can make a trigger by passing through the corners of both scintillators and not traversing the detector body at all. We can give a very poor estimate by assuming a binomial distribution for the number of detected particles (each muon is assigned the same detection probability, no matter what its momentum etc. is, which is quite a crude approximation). Then

$$\Delta(N_{\mu}^{\text{rgstd}})_{\text{stat}} = \sqrt{\frac{N_{\mu}^{\text{rgstd}} \cdot (N_{\text{event}} - N_{\mu}^{\text{rgstd}})}{N_{\text{event}}^2}}.$$

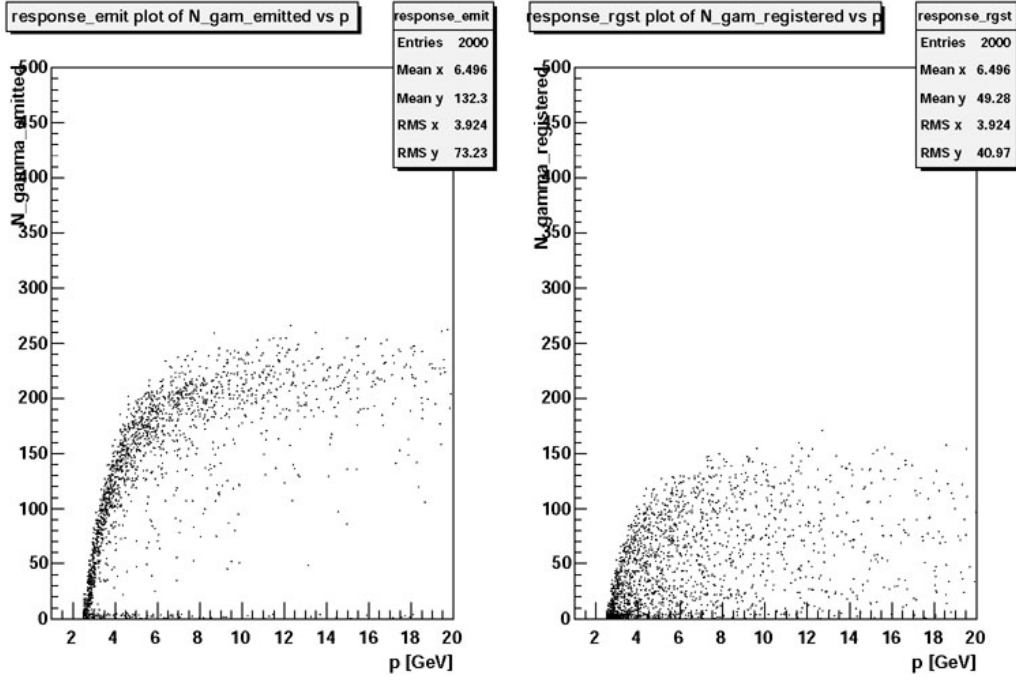


Figure 4.1: N_{γ}^{emit} and $N_{\gamma}^{\text{rgstd}}$ vs. p_{μ}

If we try this equation on some numbers, say our dataset for $P = 3 \text{ atm}$: $N_{\text{event}} = 2000$, $N_{\mu}^{\text{rgstd}} = 1842$, we obtain $\Delta(N_{\mu}^{\text{rgstd}})_{\text{stat}} = 0.1$ (!). So, even if the shape of the PDF will affect this value by 1000%, we will still get an uncertainty of only 1 (!) detected event, which is really small compared to the error $\Delta(t_{\text{passed}})_{\text{total}}$ (see next paragraph) and therefore will be *neglected* in the following discussion.

Now, let us come to the *systematic* error $\Delta(N_{\mu}^{\text{rgstd}})_{\text{syst}}$. There are several factors that play a role. First, there is a "geometrical" error, which accounts for the imperfections of the simulation program. For instance, the reflectivity of the mirror, though above 90% in real life is assumed to be 1, its shape is not a perfect ellipse etc. Second, we must assume a systematic error of approx. 5% for the manometer: $\Delta(P) \cong 0.05 P$. This leads to an error in the refractive index $\Delta(n)$ and $\Delta(N_{\gamma}^{\text{emit}})_{\text{syst}}$. Though, these two error sources will have a rather insignificant contribution mainly to the momentum region just above threshold $p_{\mu}^{\text{thresh}}(P)$ with low numbers of emitted photons N_{γ}^{emit} . This is due to the fact that the decision if a muon is registered or not is made binary: it is positive if the number of registered photons is above a threshold value $N_{\gamma}^{\text{thresh}} \doteq 1$ or more. The next, by far largest contribution arises from estimation of the detection threshold $N_{\gamma}^{\text{thresh}}$ as such. In the simulation we have assumed $N_{\gamma}^{\text{thresh}} \doteq 1$, but in reality this value can likely be in the order of 3 or even more photons. Finally, the 3 scintillator trigger will not be 100% efficient, giving an additional bias to the data.

Considering all the arguments presented above, we estimate the total error of N_{μ}^{rgstd} to approximately 15%:

$$\Delta(N_{\mu}^{\text{rgstd}}) \equiv \Delta(N_{\mu}^{\text{rgstd}})_{\text{syst}} \doteq 0.15 \cdot N_{\mu}^{\text{rgstd}}. \quad (4.8)$$

What is now the error to N_{μ}^{incid} , the number of incident muons with a momentum above 1 GeV? Since this value is not experimentally accessible and only serves for the calculation of t_{passed} , let us focus this question in the next paragraph.

Time passed in the experiment: error discussion

In the previous paragraph we have already discussed the fact that N_{event} is free of *statistical* errors, but $t_{\text{passed}} := N_{\mu}^{\text{incid}} \cdot \langle T_{1 \text{ GeV}} \rangle$ is not:

$$\Delta(t_{\text{passed}})_{\text{stat}} = \sqrt{N_{\mu}^{\text{incid}} \cdot \langle T_{1 \text{ GeV}} \rangle}, \quad (4.9)$$

which reflects the real physical situation – you can wait for, say, 2000 muons above 1 GeV, but the time you will need to collect them will fluctuate with the square root of the number of particles you wait for (in our example $\sqrt{2000}$), as we have a Poisson distribution of events in time due to a low event probability.

Yet, there is another, *systematic* uncertainty to t_{passed} , which arises from a systematic error both in $\langle T_{1 \text{ GeV}} \rangle$ and N_{μ}^{incid} .

Let us devote our attention to the error of $\langle T_{1 \text{ GeV}} \rangle$ first. It is roughly given by 15%:

$$\Delta(\langle T_{1 \text{ GeV}} \rangle) \simeq 0.15 \langle T_{1 \text{ GeV}} \rangle = 1.45 \text{ s}. \quad (4.10)$$

We come to this estimation via Gaussian error propagation from the uncertainty stated for $I_{\mu^{\pm}}(\theta = 0, p_{\mu} > 1 \text{ GeV})$ in [1, 2], being a lower normalization by 10-15%, which leads to a higher value for $\langle T_{1 \text{ GeV}} \rangle$ according to eq. 4.4; plus an additional factor of $\sim 7\%$ accounting for varying Sun activity on different time scales and clouds (water vapor plays a crucial role in energy loss due to ionization, as noticed recently in an analysis of the correlation between weather and cosmic muon rates: [2]).

Now, let us focus the systematic error to N_{μ}^{incid} , the number of incident muons with momentum above 1 GeV. It is important to know that our detector stands in the T-building on the NIKHEF compound, in the former Target Area of the LINAC (LINear ACcelerator), which was an e^{-} machine. Considering this, we may assume the thickness of the roof concrete to be 5 RADIATION LENGTHS (see [1] or [2] for its definition). This corresponds to roughly $5 \cdot 10.7 \text{ cm} \simeq 50 \text{ cm}$, which will decelerate the muons by $\langle -\frac{dE}{dx} \rangle \simeq 4.2 \text{ MeV cm}^{-1}$ on average, thus decreasing their momentum by approx. 0.2 GeV. Of course, this affects the number of incident muons N_{μ}^{incid} with momentum above 1 GeV, since the whole spectrum is shifted. The effect¹ is

$$\Delta(N_{\mu}^{\text{incid}}) \simeq 0.07 \cdot N_{\mu}^{\text{incid}}, \quad (4.11)$$

as concluded from the data in [3].

Thus, we conclude from eqq. 4.10, 4.11 for the *systematic* uncertainty to t_{passed} :

$$\begin{aligned} \Delta(t_{\text{passed}})_{\text{syst}} &= \sqrt{\{\Delta(N_{\mu}^{\text{incid}})_{\text{syst}} \cdot \langle T_{1 \text{ GeV}} \rangle\}^2 + \{N_{\mu}^{\text{incid}} \cdot \Delta(\langle T_{1 \text{ GeV}} \rangle)\}^2} \\ &= \sqrt{0.07^2 + 0.15^2} \cdot N_{\mu}^{\text{incid}} \cdot \langle T_{1 \text{ GeV}} \rangle \\ &\simeq 0.17 \cdot t_{\text{passed}}. \end{aligned} \quad (4.12)$$

Now, using eqq. 4.9, 4.12 it is an easy job to give the total error to t_{passed} :

$$\begin{aligned} \Delta(t_{\text{passed}}) &:= \sqrt{\{\Delta(t_{\text{passed}})_{\text{stat}}\}^2 + \{\Delta(t_{\text{passed}})_{\text{syst}}\}^2} \\ \Rightarrow &= \sqrt{N_{\mu}^{\text{incid}} \cdot \langle T_{1 \text{ GeV}} \rangle^2 + 0.17^2 \cdot t_{\text{passed}}^2}. \end{aligned} \quad (4.13)$$

¹There is another aspect to it: formally seen both N_{event} and N_{μ}^{rgstd} will be reduced; but the effect on N_{event} , which is assumed to be errorless, is included via N_{μ}^{incid} in t_{passed} , whereas a similar argument holds for N_{μ}^{rgstd} for the reason that it gives you the efficiency of the detector response, while the rate information is included in t_{passed} again.

Please note that in the whole discussion of this paragraph we have used that all contributing errors are independent on each other and add according to the Gaussian theorem of error propagation.

Event rates: error discussion

Now it is an easy job to give the formulas for errors on event rates. For the incident muon rate we obtain due to its definition:

$$\begin{aligned}\dot{N}_\mu^{\text{incid}} &:= \frac{1}{\langle T_{1\text{ GeV}} \rangle} \\ \stackrel{\text{eq. 4.10}}{\Rightarrow} \Delta(\dot{N}_\mu^{\text{incid}}) &= \frac{\Delta(\langle T_{1\text{ GeV}} \rangle)}{\langle T_{1\text{ GeV}} \rangle^2} = 0.15 \cdot \dot{N}_\mu^{\text{incid}} \\ &= 0.015 \text{ s}^{-1}.\end{aligned}$$

With the registered muon rate $\dot{N}_\mu^{\text{rgstd}}$ things are not much more complicated. We obtain the error $\Delta(\dot{N}_\mu^{\text{rgstd}})$ once again straight forward via Gaussian error propagation:

$$\begin{aligned}\dot{N}_\mu^{\text{rgstd}} &= \frac{N_\mu^{\text{rgstd}}}{t_{\text{passed}}} \\ \Rightarrow \Delta(\dot{N}_\mu^{\text{rgstd}}) &= \sqrt{\left\{ \Delta(N_\mu^{\text{rgstd}}) \cdot \frac{1}{t_{\text{passed}}} \right\}^2 + \left\{ \Delta(t_{\text{passed}}) \cdot \frac{N_\mu^{\text{rgstd}}}{t_{\text{passed}}^2} \right\}^2} \\ \stackrel{\text{eqq. 4.8, 4.13}}{\Rightarrow} &= \sqrt{\left\{ 0.15 \cdot \dot{N}_\mu^{\text{rgstd}} \right\}^2 + \left\{ \Delta(t_{\text{passed}}) \cdot \frac{N_\mu^{\text{rgstd}}}{t_{\text{passed}}^2} \right\}^2}.\end{aligned}\tag{4.14}$$

The discussion of the uncertainty to the total event rate \dot{N}_{total} including all charged particles is not that easy. Let us recall eq. 4.6. At first sight we might assume

$$\Delta(\dot{N}_{\text{total}}) \stackrel{?}{=} 1.82 \Delta(\dot{N}_\mu^{\text{incid}}),$$

but there is also a systematic error to the factor 1.82, which is very hard to estimate. It consists of two parts: $I_{\text{total}}^\mu / I_{1\text{ GeV}}^\mu \simeq 1.38$ and $(I_{e^\pm} + I_{p^\pm}) / I_{\mu^\pm} \simeq 0.44$. The second factor has an error of 100%, since our detector is positioned in a former accelerator building with concrete shielding, which should by design screen off electrons. The same reason will account for a significant error to the first factor. Regarding the arguments presented above we are forced to conclude, that \dot{N}_{total} is nothing more but a guide value with an error of $\mathcal{O}(100\%)$.

4.5 The simulation algorithm in detail

After the general features of the experiment have been discussed in the sections above, let us become more concrete and discuss the features of the simulation program in a more detailed way. However, this does not mean that we will cover each aspect of it. For a really detailed insight, please refer to the simulation code. You can download it from http://www.nikhef.nl/~x50/NIKHEF_proj/cher.C, it is written in C++ under ROOT, a package widely used in all fields of physics where you have to deal with statistical data analysis and simulation. It offers many more features like the possibility to display histograms in up to 3 dimensions. As in the program a lot of geometrical calculations are made, e.g. rotations

of Euclidean vectors from frame to frame, the ROOT package PHYSICSVECTOR is used. Most of their specific commands in the code are self-explaining, for details you can refer for ROOT to <http://root.cern.ch/> and to <ftp://root.cern.ch/root/doc/chapter15.pdf> for PHYSICSVECTOR.

In the following a short summary of geometrical parameters of our experiment and their definitions in the simulation program is given (for visualization, please refer to fig. 4.2 on page 28):

<code>l = 200 cm</code>	total height of the detector body
<code>l_side = 12 cm</code>	length of the sidearm measured from main trunk pipe
<code>R = 13.5 cm</code>	radius of the trunk pipe
<code>K_up = 31 cm</code>	size of the upper scintillator coincidence unit (quadratical)
<code>K_do = 31 cm</code>	size of the lower scintillator coincidence unit (quadratical)
<code>l_up = 25 cm</code>	distance of the upper coincidence unit from detector trunk
<code>l_do = 25 cm</code>	distance of the lower coincidence unit from detector trunk
<code>R_pmt = 6.25 cm</code>	radius of the PMT window and the PMT itself

Introduction to the main features of the algorithm

Before we start to introduce the simulation of each physical process, a short overview of the main features of the algorithm shall be given.

What does the simulation program do step-by-step? In the first place, the muons, i.e. their momenta and propagation tracks inside of the detector body are randomly generated using the function `muon()`. The next step is the emission of Cherenkov photons. This is done in the function `gamma()` by successive generation of randomly distributed photon emission points along the muon track and the corresponding photon directions on the Cherenkov cone. Later in `get_mirror(\vec{r}, \vec{n})`, which is called by `gamma()`, the reflection point on the mirror at the detector bottom and the propagation direction after the mirroring are calculated. Finally, in `gamma()` for each photon the decision if it is registered or not is taken. The discrimination is done on a geometrical basis, i.e. if a photon hits the detector window for the PMT at all, and on a wavelength dependent probability for a photon to trespass the glass of the window and to excite a photoelectron from the alkali cathode following its quantum efficiency. To get a better idea about the simulation steps, take a look at fig. 4.2 on page 28. There a muon track and one of the photon tracks are displayed, together with the corresponding coordinate frames, which are useful for mathematical description. The last two parts of the simulation program to be mentioned are `cher()`, the main function which calls `muon()`, `gamma()` and keeps track of the number of registered muons N_{μ}^{rgstd} etc., and `canvas()`, a rather uninteresting function responsible for the initialization of histograms in ROOT.

In the following we will refer to all function and variable names in the simulation code by a typewriter font, e.g. $|\vec{p}_{\mu}| \equiv p$.

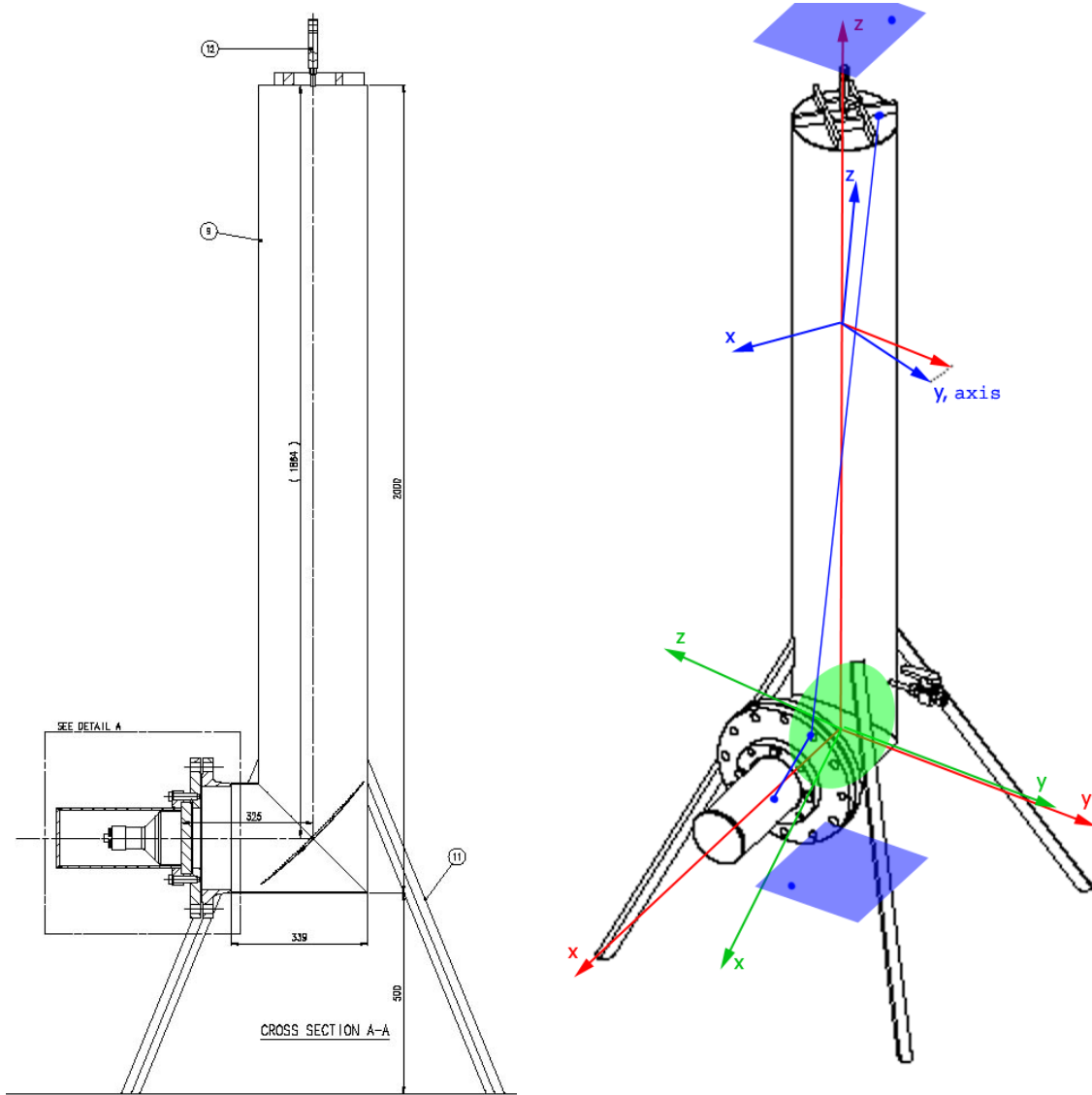


Figure 4.2: **left:** Technical drawing; **right:** Perspective drawing of the detector. The mirror is drawn in light green at the bottom of the detector, the coincidence unit on top and beneath the detector in light blue, plus an arbitrary muon trace in dark blue with the two triggering points, the entering point at the top, the exit point through the mirror and the point where to it would have been reflected, if it was a photon (the actual photons will be spread around it). Also the coordinate frames are shown: the lowest one in red is the detector frame, also at the bottom, tilted to the detector frame in green is the mirror frame, upper most in blue is the muon frame.

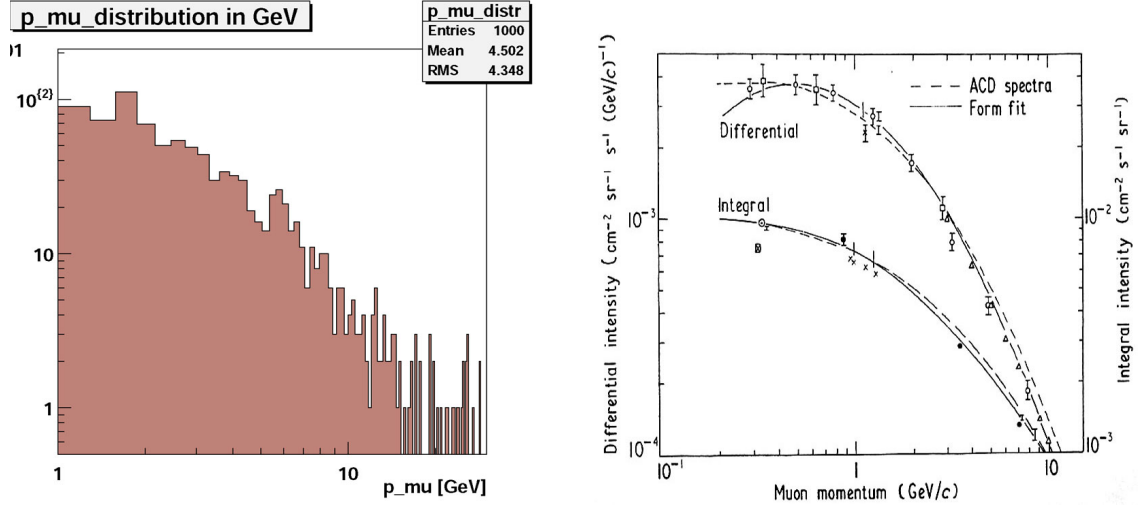


Figure 4.3: **left:** Muon momentum spectrum between 1 and 30 GeV; **right:** Muon spectrum as presented in [3]

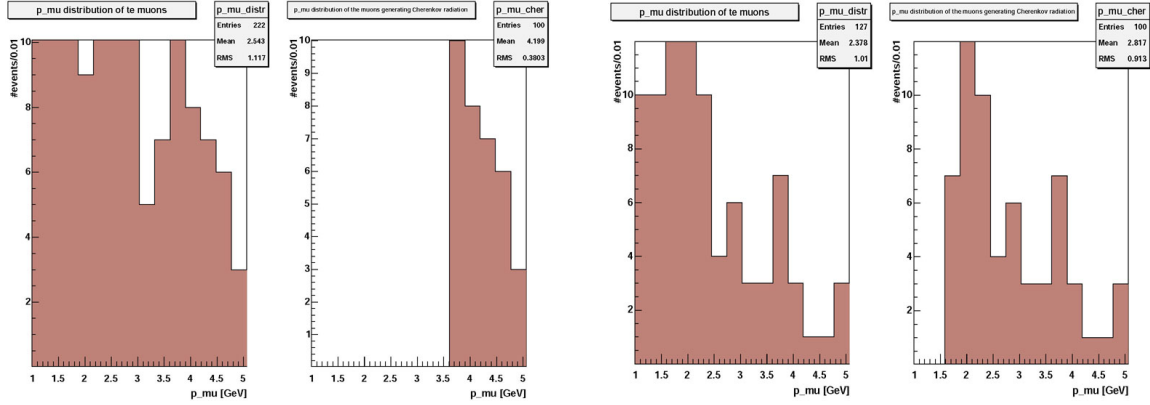


Figure 4.4: Cutoff by Cherenkov condition in momentum distribution for P=1 atm (left) and P=5 atm (right)

Generation of the muon momentum distribution: `muon()`

The muon, being an elementary particle, is fully characterized by its position in the Minkowski space x_μ and by its 4-momentum p_μ . For our purposes only the spatial coordinates \vec{x}_μ of the muon track and the absolute value of its momentum $|\vec{p}_\mu| \equiv p$ are interesting. In this paragraph a proper random generation of the latter will be focused.

As already discussed, cosmic muons follow a certain distribution $\frac{dN}{dp} \equiv dNdp$, which can be roughly parameterized as $\frac{dN}{dp} \propto p^{-2.7}$. However, this approximation has validity only in the momentum range between 10 and 1000 GeV, and becomes steadily poorer in the important range towards 1 GeV, since here the γ -factor of the muons is smaller and more muons decay on their way to the Earth surface. Thus, analytical methods cannot be used for random number generation here and the values have to be interpolated from a table. We have used a rather straight forward acceptance-rejection method. It works as follows: assume you want to generate a series of variables x which follow a certain PDF (probability distribution function) $f(x)$; you generate a pair of independent random numbers v_1, v_2 and

calculate $f(v_1)$. If $v_2 < f(v_1)$, you accept v_1 as a draw from your PDF, $x \doteq v_1$; else you restart with a new pair of v_1, v_2 .

As the table in [3] is rather not up-to-date, we decided to interpolate the data from a graph in fig. 24.4 in [2]. However, because of the $\frac{dN}{dp} \propto p^{-2.7}$ dependance $p^{2.7} \cdot \frac{dN}{dp} \equiv \text{pdNdp}$ was displayed by the graph, so each value of the table has to be divided by $p^{1.7}$. We have simulated the momentum range $|\vec{p}_\mu| \in [1, 300] \text{ GeV}$, which is a very good approximation because of the exponential drop for high energies.

Now, not every muon above 1 GeV will fulfill the Cherenkov condition 4.2. So, for each $|\vec{p}_\mu|$ the corresponding emission angle θ_{emiss} is calculated. Logically, the program exits the while loop only in the case $\theta_{\text{emiss}} > 0$.

You can compare the generated momentum spectrum with a figure from [3] in fig. 4.3 on page 29. Further, in fig. 4.4 the effect of Cherenkov condition discrimination can be seen for $P=1$ and 5 atm.

Generation of muon incidence points & propagation directions: `muon()`

After the absolute momentum of the muon is generated, its track through the detector is simulated. For a proper simulation of this part we do not need anything else but a starting point and a propagation direction. Since we use a coincidence unit anyway, it makes sense to generate randomly an entering point at the upper coincidence unit, `r_mu_up` and an exit point at the lower one `r_mu_do`. The difference of these two will give us the propagation direction $\mathbf{n}_\mu = (\mathbf{r}_{\text{mu_do}} - \mathbf{r}_{\text{mu_up}}) / |\mathbf{r}_{\text{mu_do}} - \mathbf{r}_{\text{mu_up}}|$. Clearly, it is pragmatical to choose the starting point for further simulation steps to be the trespassing point of the muon through a plane defined by the top of the detector body. For this purpose we introduce the path length parameter s (s , in cm), so that $\vec{x}_\mu(s) \equiv \mathbf{r}_\mu(s) = \vec{r}_{\text{start}} + s \cdot \mathbf{n}_\mu$ and pass \vec{r}_{start} to the function `gamma()` by setting $\mathbf{r}_\mu(s) \Big|_{s=\text{trespass}} \doteq \vec{r}_{\text{start}}$.

Generation of photon emission points along the muon track: `gamma()`

By now we have generated muons trespassing our detector, but nothing else happened yet. In the next step we will implement the emission of Cherenkov radiation. What we want to know at the end is if the photons hit the PMT window and which wavelengths they have, since its transitivity and the quantum efficiency of the PMT – in other words the registration probability – will depend on it. To approach the problem properly, we have to keep two things in mind: on the one hand, the *wavelength* of emitted photons will follow a certain PDF $\frac{dN}{d\lambda}$; on the other hand the *spatial points of emission* will be randomly distributed along the muon track and their total number will depend on the probability to emit Cherenkov radiation per pathway $\frac{dN}{dx}$. Both PDF's can be calculated by the virtue of a formula for $\frac{d^2N}{d\lambda dx}$ (as given in eq. 4.3): $\frac{dN}{d\lambda} = \int dx \frac{d^2N}{d\lambda dx}$, $\frac{dN}{dx} = \int d\lambda \frac{d^2N}{d\lambda dx}$.

Let us consider the "spatial" part of the problem. As argued above, we start with

$$\frac{dN}{dx} = K \cdot \left(1 - \frac{1}{\beta^2 n_{\text{CO}_2}^2} \right) \quad \text{with } K[\text{cm}] := 10^7 \cdot 2\pi\alpha \cdot \left(\frac{\lambda_{\text{max}} - \lambda_{\text{min}}}{\lambda_{\text{max}} \lambda_{\text{min}}} \right), \quad \lambda \text{ in nm},$$

where $\lambda_{\text{min}}, \lambda_{\text{max}} = 300, 600 \text{ nm}$ are the wavelengths imposed by limited properties of our apparatus, e.g. transmittancy of borosilicate glass of the window for the PMT. Now we have the probability for photon emission per pathway of 1 cm. The next question to deal with, is how to distribute the emission points properly along the muon track. Clearly, the $\frac{dN}{dx}$ PDF

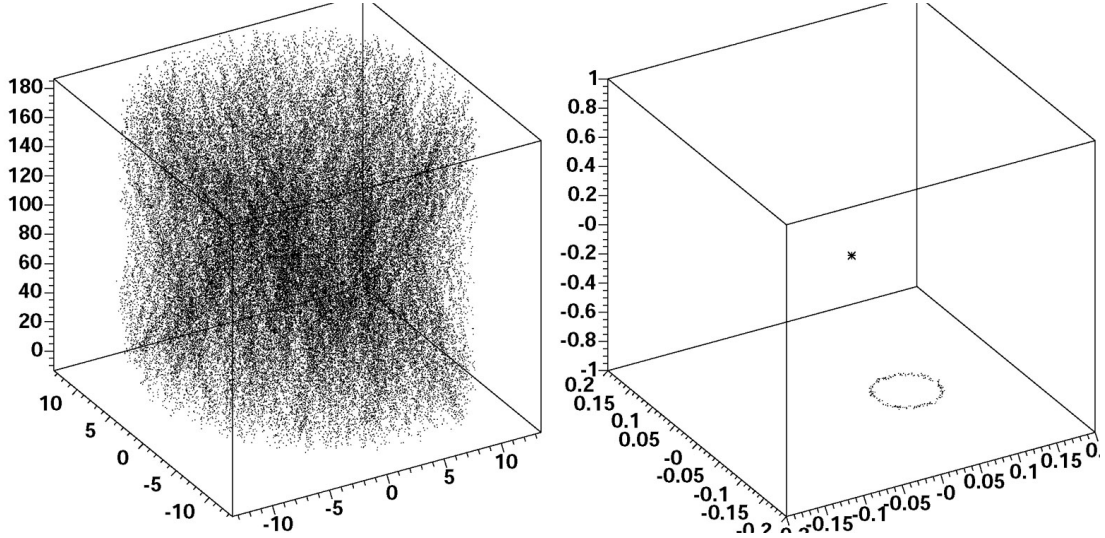


Figure 4.5: **left:** 3-Dimensional distribution of photon emission points for 1500 muons at $P = 4$ atm inside of the detector pipe. Its round shape is clearly visible; at the bottom, tilted by 45° , the mirror can be seen. Please remark, that the scales for x-y-plane and z-axis are different; **right:** Distribution of photon propagation directions \vec{n}_γ for *one* muon. In this diagram the scales of the axes are not the same as well.

will be uniform (i.e. will have a constant value). On the other hand, the number of emitted photons will fluctuate over a certain pathway. To approach the problem, we will divide the muon track in small steps of $\Delta x \equiv \mathbf{dx}$, with Δx being small enough, so that we can assume a Poisson distribution for the number of emitted photons per Δx ; we go even further with approximations and set Δx in such a way that $\frac{\Delta N}{\Delta x} = 0.1 [\Delta x^{-1}]$, with such a choice we can neglect cases where more than 1 photon is emitted, due to their extremely low probability. Then $\Delta x = \Delta N / \frac{dN}{dx} = 0.1 / \frac{dN}{dx}$ and we can simulate radiation emission by generating one photon per Δx with a probability of 0.1. Thus, we "propagate" the muon along its track in a for-loop by $\vec{r}_\gamma(s) = \vec{r}_\mu + s \cdot \vec{n}_\mu$, where s is increased in steps of Δx and generate a photon if the following conditions are fulfilled: first, a random number generated in the range $[0, 1]$ lies between 0 and 0.1; second, the muon is inside of the detector body (orthogonal distance to the detector pipe axis is smaller than R , the inner radius of the pipe). But how do we tell the programm, when the emission is to stop, i.e. when the muon exits the detector at its bottom? Let us anticipate the function `get_mirror(\vec{r}, \vec{n})` first. For each pair of \vec{r}, \vec{n} it calculates the point $\vec{r}_{\text{mir}} \equiv \mathbf{r_mir}$, at which a particle with these parameters will trespass the mirror at the detector bottom and the propagation direction $\vec{n}_{\text{mir}} \equiv \mathbf{n_mir}$ after the mirroring. Thus, if we determine $\mathbf{r_mir}$ for the mirror and calculate the path length parameter s for this point and divide s by Δx , we will know where to stop the emission, i.e. when to stop the for-loop. You can get an idea of how the photon emission points are distributed in fig. 4.5 on page 31. Furthermore, we have checked that the number of emitted photons N_{emit} for fixed muon momentum $|\vec{p}_\mu|$ and pressure P indeed fluctuates like $\sqrt{N_{\text{emit}}}$, as it should be the case for a Poisson distribution.

Simulation of the Cherenkov emission cone: `gamma()`

So far we have enormously proceeded in understanding the simulation: we have modelled muons and their traces, we know *how many* and *where* photons will be emitted.

Next, we have to deal with assigning the photons a *propagation direction*. Clearly, the directions of the photons \vec{n}_γ lie on the Cherenkov cone. It is easiest to describe the emission in the muon frame first, and to transform the results from the muon frame to the detector frame afterwards. In the muon frame things look rather simple: we can restrict the propagation directions to the Cherenkov cone by setting the $\theta_{\vec{n}_\gamma}$ -value of \vec{n}_γ in polar coordinates to $\theta_{\vec{n}_\gamma} \doteq \pi - \theta_{\text{emiss}}$ ² and distribute them *on* the cone by generating the $\phi_{\vec{n}_\gamma}$ -values randomly from $[0, 2\pi)$.

All we have to do now is to transform \vec{n}_γ from the muon frame to the one of our detector. The muon frame (blue) is defined in the detector frame (red) by two conditions (see fig. 4.2 on page 28): first, its z_μ -axis is given by the negative propagation direction of the muon $-\vec{n}_\mu$, which fixes two of three parameters for a rotational transformation in 3 dimensions; second, its y_μ -axis lies in the x - y -plane of the detector frame and is given by $\vec{y}_\mu := -\vec{z} \times \vec{n}_\mu = \vec{z} \times \vec{z}_\mu$. Here \vec{z} is the z -axis of the detector frame, while \vec{z}_μ is the z -axis of the muon frame. Thus, the transformation is given by two³ successive rotations: around the y_μ -axis in the muon frame and around the z -axis of the detector frame. Now, the ϕ -values of \vec{n}_γ are distributed randomly anyway. In other words, the second rotation does nothing else but manipulate a random variable, which is cyclic, by a fixed value. So for our purposes it is sufficient to perform only one rotation around the y_μ -axis in the muon frame, which is done with the same parameters to every generated photon for a fixed muon track. To visualize this process see fig. 4.5 (right) on page 31.

Registration of Cherenkov photons: `gamma()`

Now that we know all propagation parameters of Cherenkov photons there are just two more steps before their final registration. Geometrically seen, all we want to know is if they hit the PMT window or not. After they are mirrored by the function `get_mirror(\vec{r}, \vec{n})` and we know the new starting point \vec{r}_{mir} and propagation direction \vec{n}_{mir} , we calculate straight forward the propagation parameter s for the photon to hit the wall with the PMT window. Next, we determine the impact point $\vec{r}_{\text{incid}}^\gamma \equiv \text{r_gamma_inc} = \vec{r}_{\text{mir}} + s \cdot \vec{n}_{\text{mir}}$, and from it its distance to the axis through the middle of the PMT window, which we discriminate at $R_{\text{PMT}} = 6.25 \text{ cm}$:

$$(r_{\text{incid}}^\gamma)_y^2 + (r_{\text{incid}}^\gamma)_z^2 \stackrel{!}{<} R_{\text{PMT}}^2.$$

In other words, we can tell now if a photon *can* be detected or not.

Logically, the last step is to tell if a photon *will* be detected or not. For this we need to generate randomly the photon wavelength λ and to look up the detecting efficiency $P_{\text{detect}}(\lambda) \equiv \text{P}$ in a table.

To perform the wavelength generation we need the PDF for the wavelength $\frac{dN}{d\lambda}$. We use the relation $\frac{dN}{d\lambda} = \int dx \frac{d^2N}{d\lambda dx}$ and eq. 4.3 again. Trivially, we obtain $\frac{dN}{d\lambda} \propto \frac{1}{\lambda^2}$. Here the equation for the cumulative distribution $N(\lambda) = \int_{\lambda_{\text{min}}}^{\lambda} d\lambda' \frac{dN}{d\lambda'}(\lambda') = \frac{1}{\lambda_{\text{min}}} - \frac{1}{\lambda}$ can be solved analytically for λ and thus we use an analytical method for the random wavelength generation. It works as follows: we generate a uniform random value for the cumulative distribution N_{rnd} from the interval $[N(\lambda_{\text{min}}), N(\lambda_{\text{max}})]$, set it equal to $N(\lambda) = N_{\text{rnd}}$ and

²Note that in our case the propagation direction of the muon points to an opposite direction of the z_μ -axis

³A general rotation is defined by three so-called Euler angles, here we have only two of them, since it is a special case (see second condition).

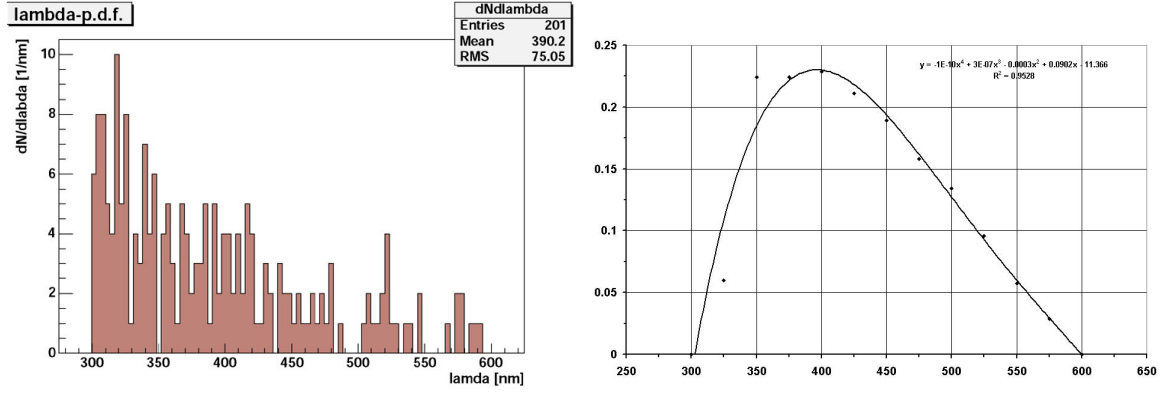


Figure 4.6: **left:** Wavelength distribution $\frac{dN}{d\lambda}(\lambda)$ for Cherenkov photons; **right:** Detection efficiency P_{detect} .

solve this equation for λ , which will then be properly distributed:

$$\lambda = \frac{1}{\frac{1}{\lambda_{\min}} - N_{\text{rnd}}}.$$

The results of this method are demonstrated in a histogram in fig. 4.6 on page 33.

Let us focus on the detecting efficiency $P_{\text{detect}}(\lambda) \equiv P$ in the next lines. It is a combination of the transmittance probability through the PMT window, which is made of 2 cm thick borosilicate glass, and the quantum efficiency of the PMT. Since both effects are not correlated we can combine them to a new value $P_{\text{detect}}(\lambda)$ by simple multiplication. The resulting graph can be seen in fig. 4.6. Obviously, the smartest way to "look up" a detection efficiency for a certain wavelength would be from a polynomial, Taylor-approximated to the values of the table to a sufficiently high order (4th). But we should keep in mind that we will have to perform this action for each photon, with about 50 per event of them arriving at the window on average, so we decided for a less CPU-time consuming lookup in a table via if-conditions.

Mirroring of the emitted Cherenkov photons: `get_mirror(\vec{r}, \vec{n})`

We are almost finished with setting up the simulation now, the only missing part is the *mirroring process* which we have left out so far. You may already have guessed it: there is nothing physically relevant to this function, all it is about are geometrical considerations. So let us apply a citation of Landau here: *"This calculation is in principle trivial, it is easier to do it by yourself, than to follow the presentation of the solution"* and just give a brief outline of how things work here.

The first "boundary condition" is the parabolic shape of the mirror (with different quadratic coefficients a, b for the both directions, the smaller one, a being exactly $\frac{1}{2}$ of the larger one: $a = \frac{1}{2}b$, since the mirror should focus perfectly while tilted by 45°), so it is easiest to transform the generation point \vec{r}_γ and the propagation direction \vec{n}_γ of the photon into the mirror frame (marked green in fig. 4.2 on page 28) by rotating them by 45° around the y -axis. Now we have a classical geometrical problem – to calculate the point of intersection for a straight line and a parabolic surface. This calculation is done by means of the path length parameter s again. Afterwards we check if the photon is on the physical mirror surface, which is limited in its size unlike the mathematical problem. Should this not be the

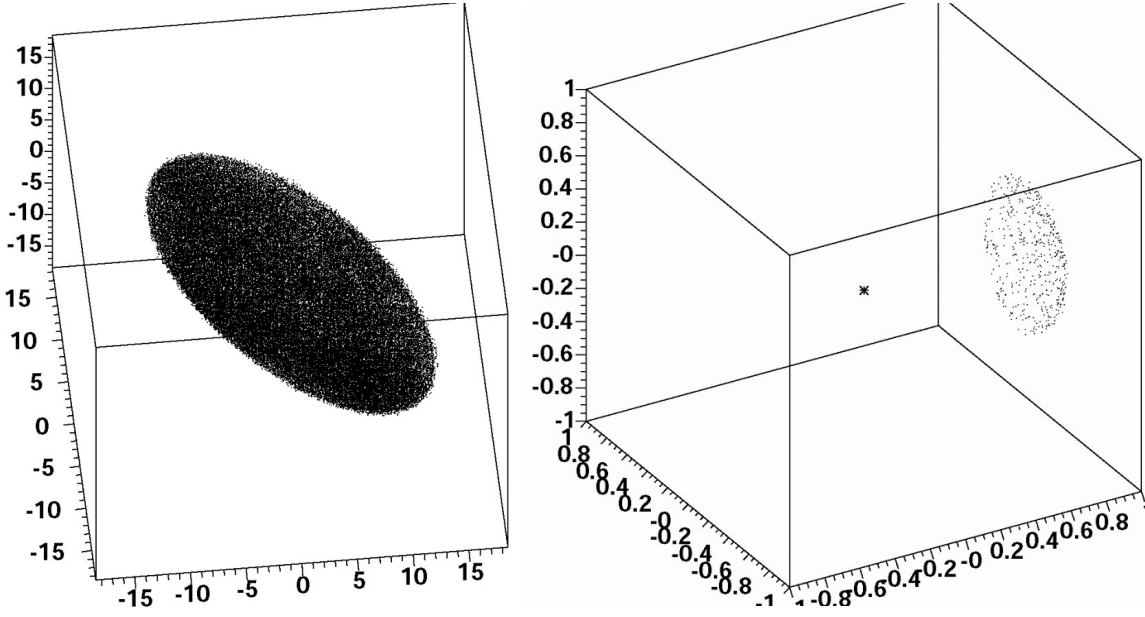


Figure 4.7: **left:** Distribution of mirroring points \vec{r}_{mir} ; **right:** Distribution of propagation directions \vec{n}_{mir} after the mirroring.

case, the photon is lost. You can get an idea about the distribution of mirroring points on the mirror surface on fig. 4.7 on page 34.

We know already *where* the mirroring happens, thus the new starting point \vec{r}_{mir} . What is still missing is the new *propagation direction*. For this we need the orthogonal vector to the surface of the mirror \vec{n}_{orth} . Once we have it, the calculation is fairly easy:

$$\vec{n}_{\text{mir}} = \vec{n}_{\gamma} - 2(\vec{n}_{\gamma} \cdot \vec{n}_{\text{orth}}) \cdot \vec{n}_{\text{orth}},$$

as follows trivially from geometric considerations. The only tricky point is to calculate the orthogonal vector to the mirror surface at the point \vec{r}_{mir} : $\vec{n}_{\text{orth}}(\vec{r}_{\text{mir}})$. It can be accessed via the following relation:

$$\vec{n}_{\text{orth}} = \vec{n}_{\text{grad}} \times \vec{n}_{\text{equal}},$$

where \vec{n}_{grad} is the (3-dimensional) gradient vector to the parabolic surface and \vec{n}_{equal} is the tangential vector to the curve of equal level *on* the parabolic surface in z -direction, thus the solution to $z_{\text{equal}} = \sqrt{x_{\text{equal}}^2 - y_{\text{equal}}^2} = \text{const.}$ Geometrical argumentation yields (except for degenerate cases like $r_{\text{mir}}^y = 0$):

$$\begin{aligned} \vec{n}_{\text{equal}} &= \frac{(\pm 1, \mp C_2, 0)^t}{|(\pm 1, \mp C_2, 0)^t|} \quad \text{for } r_{\text{mir}}^y \begin{cases} < \\ > \end{cases} 0 \quad \text{with } C_2 = \frac{a}{b} \cdot \frac{r_{\text{mir}}^x}{r_{\text{mir}}^y}; \\ \vec{n}_{\text{grad}} &= \frac{\left(n_{\text{equal}}^y, -n_{\text{equal}}^x, 2(a \cdot r_{\text{mir}}^y - b \cdot r_{\text{mir}}^x) \right)^t}{\left| \left(n_{\text{equal}}^y, -n_{\text{equal}}^x, 2(a \cdot r_{\text{mir}}^y - b \cdot r_{\text{mir}}^x) \right)^t \right|}. \end{aligned}$$

Now all we have to do is to apply the inverse rotation by 45° to go back to the detector frame. You can see a distribution of propagation directions \vec{r}_{mir} after the mirroring in fig. 4.7.

4.6 Event rates predicted by the simulation

After having presented the event generation and detector simulation algorithms we are ready to discuss the predictions given by our simulation program. These predictions will be a basis for the discussion of our measurements in chapter 7: RESULTS on page 59. For definitions of the predicted values please refer to section 4.4: INTRODUCTION OF VALUES REPORTED BY THE SIMULATION PROGRAM on page 21. In particular t_{pass} is calculated via eq. 4.5, its error $\Delta(t_{\text{pass}})$ via eq. 4.13, \dot{N}_{rgstd} via eq. 4.7, its error $\Delta(\dot{N}_{\text{rgstd}})$ via eq. 4.14.

Before we come to the actual data and predictions, you might find it interesting to take a look at a survey of the most important characteristic values and parameters for different pressures of $P = 1, 2, 3, 4, 5$ atm in table 4.1 first. The probably most interesting values are stated in the last two columns: the momentum threshold for emission of Cherenkov radiation p_{thresh} and the average number of emitted photons $\langle N_{\text{yield}} \rangle_{\text{opt}}$ for optimal conditions ($\beta \doteq 1$, the pathway of the muon inside of the active medium being the full detector length l).

P [atm]	n	θ_{max} [rad]	β_{thresh}	p_{thresh} [GeV]	$\langle N_{\text{yield}} \rangle_{\text{opt}}$
1	1.00041	0.029	0.9996	3.69	125
2	1.00082	0.040	0.9992	2.61	250
3	1.00123	0.050	0.9988	2.13	375
4	1.00164	0.057	0.9984	1.84	500
5	1.00205	0.064	0.9980	1.65	625

Table 4.1: Characteristic values for our experiment

We have made several runs of the simulation program for the pressures above. The number of events and therefore the statistical basis differs for different P , depending on needed vs. available calculation time (clearly, a run with a high refractive index $n(P)$ will consume more CPU time, as then more photons are to be generated along the muon track due to a higher $\frac{dN}{dx d\lambda}$). You can view all the predicted values including their errors in table 4.2. Later, after having taken data with the detector, we have also run the simulation program with the same pressures and refractive indices we have actually run the detector with⁴. In order to do that we also implemented in the simulation the fact that the detector was used with a mixture of air and CO₂ gas, and that the total pressure and refractive index for each run was calculated from the gas composition on that run. This would be fully explained in section 6.2. You can view the predictions from these later runs in the lower part of the table.

You might regard it to be interesting to take a look at the numbers of *emitted* and *registered* Cherenkov photons for different muon momenta p_{μ} in fig. 4.8 on page 37. What makes these diagrams worth mentioning is the fact that they give quite a good idea about the detection probability for different p_{μ} . What we see for both the emitted and registered photons is a strong, $1 - \exp(-p_{\mu})$ - like rise for low muon momenta. Even more interesting is the fact that the average number of *registered* photons is significantly smaller than the other one. Furthermore, an important difference are the many points below the main "curve" for *registered* photons, which is due to the fact that many of them will not be geometrically detected.

⁴To set a certain pressure, say 2 atm, was not easy because we did not have a second manometer, whereas using the one on the gas bottle was not possible due to the fact that there was a not predictable pressure drop along the gas filling line

P [atm]	$(n-1) * 10^6$	N_{μ}^{incid}	N_{event}	N_{μ}^{rgstd}	t_{pass} [s]	$\Delta(t_{\text{pass}})$ [s]	\dot{N}_{rgstd} [s ⁻¹]	$\Delta(\dot{N}_{\text{rgstd}})$ [s ⁻¹]	$\langle T_{\text{rgstd}} \rangle$ [s]
1	410	11766	5000	4208	113753	19366	0.037	0.008	27.0
2	820	3517	2000	1782	34002	5809	0.052	0.012	19.1
3	1230	3099	2000	1842	29961	5122	0.061	0.014	16.3
4	1640	2022	1500	1391	19549	3352	0.071	0.016	14.1
5	2050	2564	2000	1849	24789	4242	0.075	0.017	13.4
2.7	1041.2	3212	2000	1797	31053	5307	0.058	0.013	17.2
2.7*	1143.89	3117	2000	1827	30135	5151	0.060	0.014	16.7
2.2	958.38	3295	2000	1797	31856	5444	0.056	0.013	17.9
1.0	436.22	4538	2000	1692	43873	7487	0.038	0.009	26.3
1.4	614.62	4043	2000	1767	39088	6673	0.045	0.010	22.2
1.8	793.02	3562	2000	1801	34437	5883	0.052	0.012	19.2
2.2	971.42	3236	2000	1808	31285	5347	0.058	0.013	17.2
2.6	1149.82	2990	2000	1798	28907	4943	0.062	0.014	16.1

Table 4.2: Values predicted by the simulation program. At the lower part of the table reported values for simulations done with gas composition and refractive index similar to the actual detector runs. * Although the first two runs were done with the same total pressure, the air-CO₂ mixture was different, which leads to different refractive index and simulation output. This is also true for runs 3 and 7.

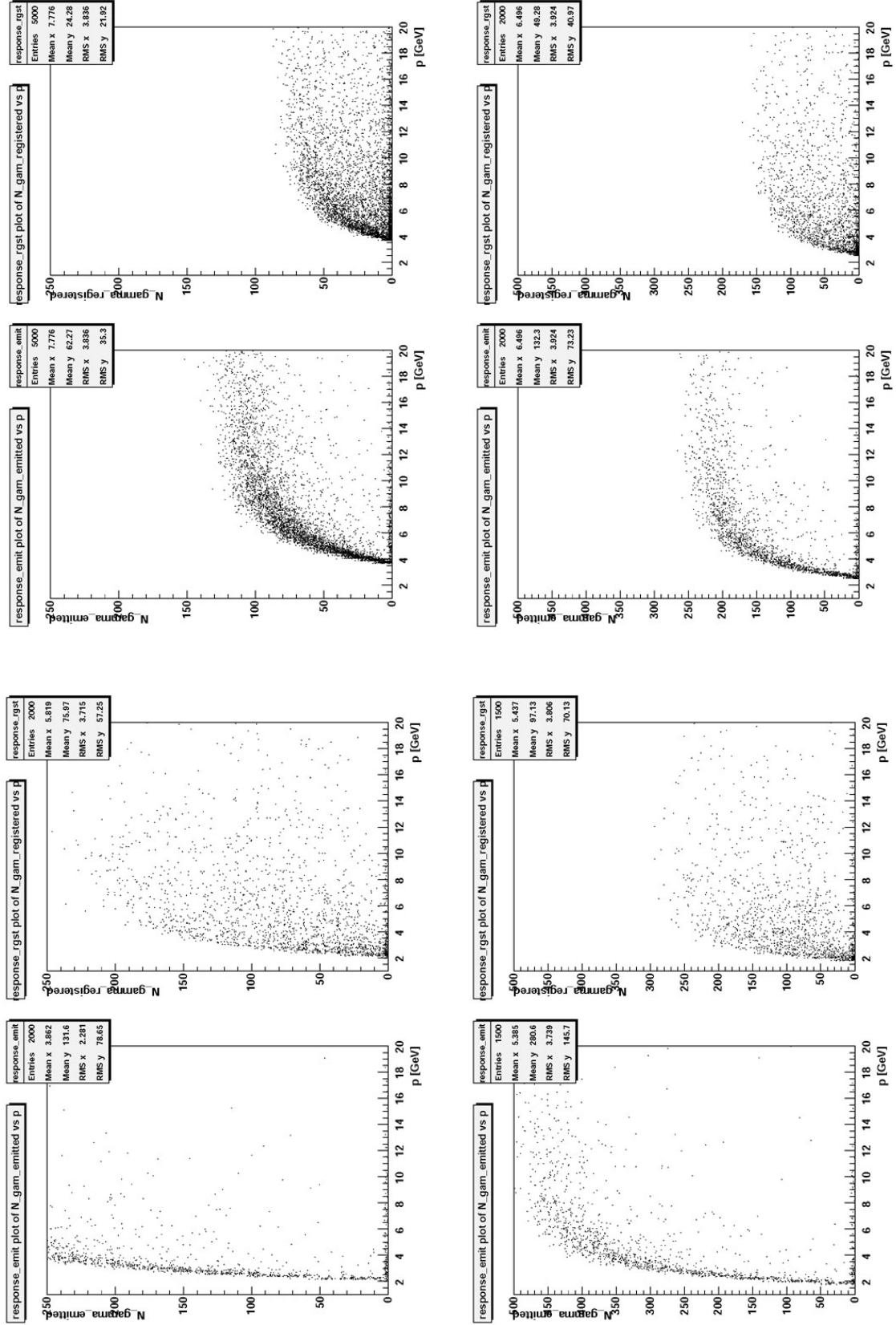


Figure 4.8: Numbers of *emitted* and *registered* Cherenkov photons for different muon momenta p_μ for $P = 1, 2, 3, 4$ atm (top left, top right, bottom left, bottom right with *this* page orientation)

Chapter 5

Setup and Building of the Detector

In this chapter we present the setup of the detector in detail. The dimensions are already known from the discussion in chapter 4: SIMULATION on page 17. First we will report about the setup itself, later about the different components in it.

5.1 Detector setup

5.1.1 Basic setup and detector quality

As we have seen from the discussion in chapter 4, Cherenkov radiation is a very weak source of photons. Therefore light collection and detection must be as efficient as possible in our experiment. As a radiator we chose to use an aluminum tube filled with CO₂ gas. For the collection of the Cherenkov light we use a parabolic mirror which focusses the light onto the main PMT.

We know from chapter 4 that the number of photoelectrons (p.e.) emitted from the cathode of the PMT in a wavelength range from λ_1 to λ_2 is given by

$$N_{p.e.} = 2\pi\alpha L \int_{\lambda_1}^{\lambda_2} d\lambda \frac{1}{\lambda^2} QE(\lambda) \epsilon_{\text{det}}(\lambda) \sin^2 \theta_{\text{emiss}}(\lambda) \quad (5.1)$$

where $\epsilon_{\text{det}}(\lambda)$ is the detection efficiency defined below, $QE(\lambda)$ the quantum efficiency of the photomultiplier, L the length of the detector and

$$\sin^2 \theta_{\text{emiss}}(\lambda) = 1 - \frac{1}{\beta^2 n(\lambda)^2}$$

with $\theta_{\text{emiss}}(\lambda)$ the Cherenkov opening angle discussed earlier, n index of refraction of the radiator (as a function of both pressure P and wavelength λ) and β the velocity of the incoming particle.

The efficiency $\epsilon_{\text{det}}(\lambda)$ is defined by the product of the transmittivity curve $T_{\text{rad}}(\lambda)$ of the radiator, the reflectivity of the mirror $R(\lambda)$ and the transmittivity curve $T_{\text{win}}(\lambda)$ of the window in front of the main PMT

$$\epsilon_{\text{det}}(\lambda) = T_{\text{rad}}(\lambda) R(\lambda) T_{\text{win}}(\lambda)$$

In our case, the index of refraction is approximately constant over the accessible PMT range, [300,600]nm, i.e. $n(\lambda) = \langle n(\lambda) \rangle$. Furthermore, we put $QE(\lambda)$ and $\epsilon_{det}(\lambda)$ outside of the integral in eq. 5.1 and use their maximum values¹. Then we can rewrite eq. 5.1 as

$$N_{p.e.} \approx L N_0 \langle \sin^2 \theta_{\text{emiss}}(\lambda) \rangle \quad (5.2)$$

where

$$N_0 = 2\pi\alpha QE(\lambda)_{\text{max}} \epsilon_{\text{det}}(\lambda)_{\text{max}} \int_{\lambda_1}^{\lambda_2} d\lambda \frac{1}{\lambda^2} \quad (5.3)$$

is the Cherenkov quality factor of the detector. So in order to optimize the response of our detector we need to work on a design which maximizes this parameter.

5.1.2 Mechanical setup

Because of the small value of $\sin^2 \theta_{\text{emiss}}(\lambda)$ and the usually low values of N_0 , in order to have a sufficient number of photoelectrons emitted in the PMT, gaseous Cherenkov counters are usually rather long. Taking into account the limitations mentioned in chapter 4, we decided to use a total radiator length of 2m. Then eq. 5.2 can be written as

$$N_{p.e.} \approx QE(\lambda)_{\text{max}} \epsilon_{\text{det}}(\lambda)_{\text{max}} N \quad (5.4)$$

where N is the photon yield given by eq. 4.4.

The complete setup is shown in fig. 5.1. The external structure of the detector consists of a tube of aluminum with an outer diameter of 26.8cm. At the top, the tube is closed with an aluminum plate of 2mm thickness. According to a simulation done by the NIKHEF engineering department this plate needed to be reinforced with a couple of metal strips (7) to stand pressures up to 10 atm in order to have a safety factor of 2 (see fig. 5.2 for the result of this simulation).

At the end of the side arm of the tube a flange (8) is welded which supports the main PMT (3) and the window (4) in front of it. Finally the main PMT is enclosed by a plastic housing (5) to prevent light from outside reaching it. To keep the PMT fixed at its original position we support it by surrounding it with construction foam.

The complete setup is enclosed by a metal rack (6) which supports the three scintillators. These are placed at a fixed position, 25cm above and below the Cherenkov detector. The rack is equipped with wheels so it could slide easily in and out of its place in case there is work to be done on the detector body. Photos of the detector and more detailed mechanical drawings can be found at [8].

5.1.3 The gas system

To supply CO₂ gas into the detector we use a standard gas bottle. Since the counter will be operated at different pressures, we need to provide different overpressures (0.4/0.8/1.2 and

¹Continuous spectra could not be found, therefore we use the upper limit of these parameters.

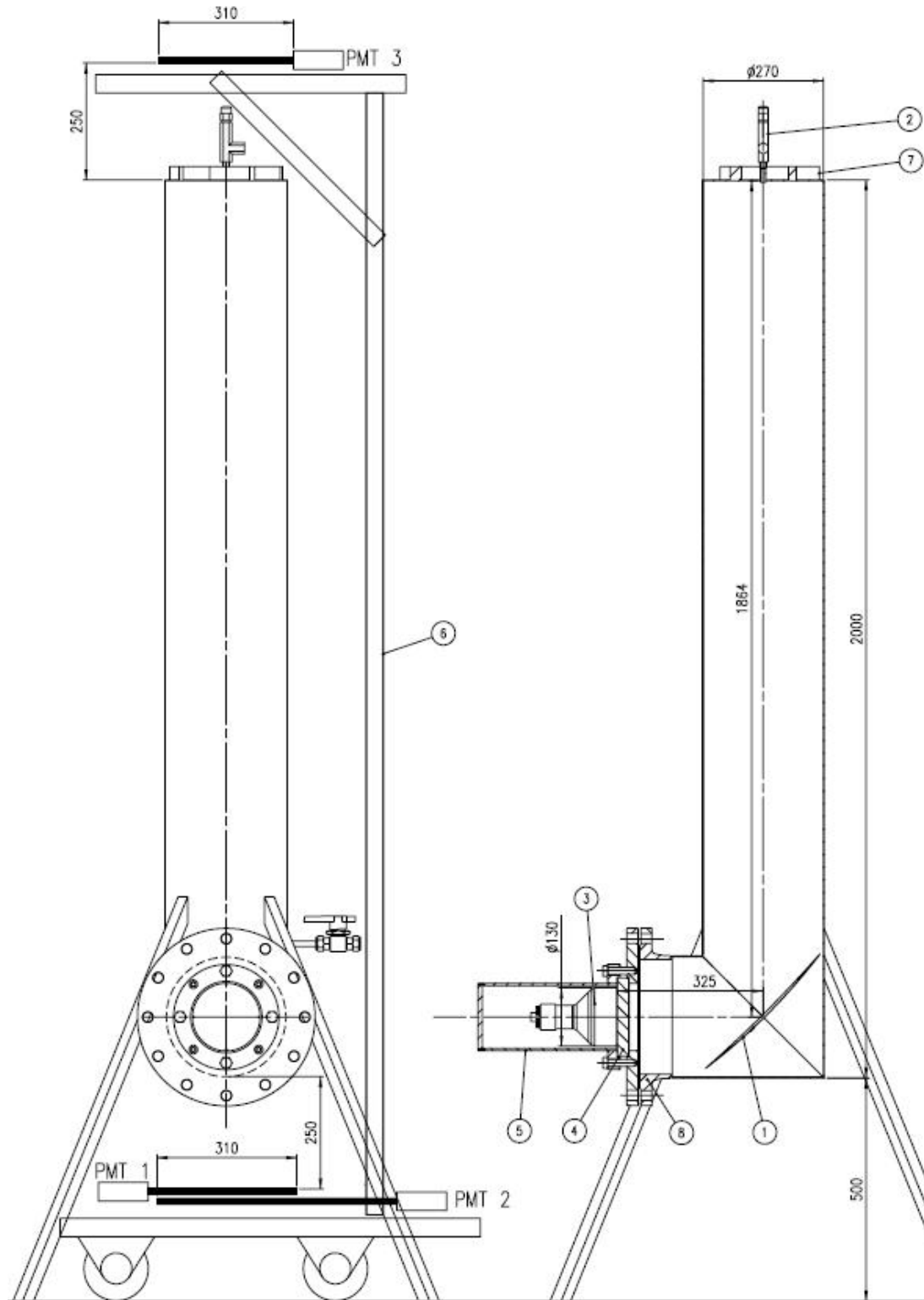


Figure 5.1: Mechanical setup. Left shows a front view of the detector, on the right is a side view. A particle enters the scintillator PMT3 from above, passing the radiator and finally the two scintillators below. Cherenkov light is reflected by a mirror (1) and focussed on the main PMT (3). Also seen are the housing of the main PMT (5), the glass window (4) held by the flange (8), the pressure safety valve (2) and the metal rack (6).

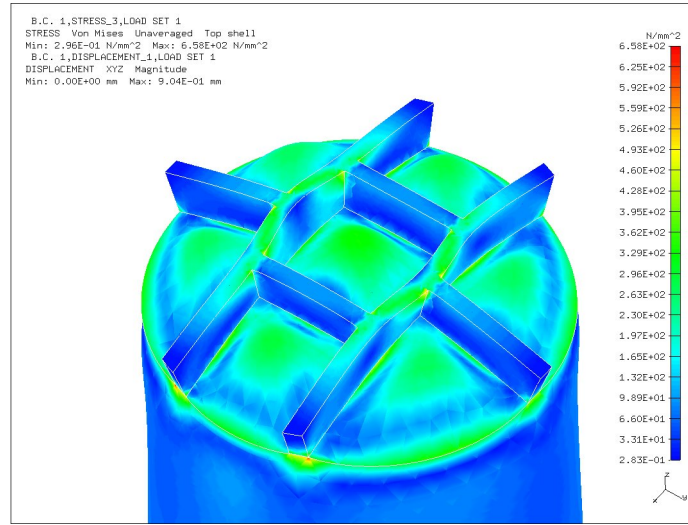


Figure 5.2: Result of the simulation to analyse the stress at the top part of the detector, up to a pressure of 10 atm. The areas with large stress on them are shown by the brighter areas (in green) on the tube cover and at the sides, at the edges of the metal strips by small spots (in red), with maximum stress of $5.92 \cdot 10^2 \text{ N mm}^{-2}$.

1.6 atm).

We have connected the gas bottle to the gas inlet at the bottom of the detector.

At the top part of the detector, a safety valve (5) is used, which is set up to release an over pressure larger than 6 atm. To ensure the gas purity we need to get rid of the air that is still inside the detector. This is done by removing the safety valve on top and using the remaining hole as the outlet. We let the CO₂ gas flow in from below and the air to go out from above. Because CO₂ is 1.5 times heavier than air, we know that after flushing, most of the air inside the detector is removed. When we are finished, we close the outlet by placing the safety valve back in its place. By letting the gas flow in from the bottle, we raise the pressure to the desired value. After we have reached the desired value, we keep the inlet valve open to establish a balance between the pressure in the detector and the one adjusted with the pressure regulator at the outlet of the bottle.

5.1.4 Electronic setup

Coincidence unit

We have placed one quadratic scintillator 25cm above the top of the detector. Two larger quadratic scintillators were placed 25cm beneath the bottom of the detector, in such a way that their overlapping area equals the area of the upper scintillator. Each scintillator has a PMT connected to it which collects the light from the scintillator and gives an electronic signal; these are PMT1, PMT2 and PMT3. The output signal cables of the three PMTs are fed into an electronic coincidence unit. The coincidence unit gives an output signal only if the three PMTs had a signal at the same time. So, when the coincidence unit gives an output signal it means that a charged particle has traversed through the entire detector body, top to bottom, and assuming it is energetic enough, it has emitted Cherenkov radiation inside the pipe. Therefore we use the signal from the coincidence unit as a trigger to our read-out system.

Read-Out system

The main photomultiplier tube of the Cherenkov counter is connected to a computer through a read-out card. The output of the coincidence unit is also connected to the same read-out card. To read and save the data from these two data channels we use a LabVIEW program installed on our computer. The program was written by the NIKHEF project students of winter 2003, who had built a water Cherenkov detector [7]. We use the three scintillators' coincident signal as a trigger to the program. Whenever the program gets a trigger it saves into a text file the values from the two data channels during a $1\mu\text{s}$ time window, starting 200nsec before the trigger and continuing 800nsec after the trigger. (Saving the pre-trigger is essential as the Cherenkov signal starts before the trigger, saving the data long after the trigger and signal is useful as we need to know the normal noise level). Later on we use the text file to perform the data analysis.

5.2 Components

5.2.1 Scintillators

In our coincidence unit we use three organic scintillators. Organic scintillators can be classed into three types, crystalline, liquid and plastic. In our case we are using the latter, which are widely used in high energy physics.

When a high energy charged particle crosses the scintillation medium it loses energy by exciting the molecules into higher energy levels. Some of the molecules will release a small fraction ($\sim 3\%$) of this energy as optical photons, this process is called scintillation. Most of the excitation energy however, is given in the form of heat and lattice vibrations. Virtually all plastic scintillators contains a base of either PVT (polyvinyl-toluene) or PS (polystyrene) that contains aromatic rings. The base contain binary or ternary solutions of selected fluors. These fluors have two main functions: (1) to efficiently re-radiate absorbed energy at wavelengths where the base is more transparent (wave-length shifter) and (2) to increase the light yield of the scintillator. The scintillator efficiency is defined as the fraction of deposit energy that transfers to radiation. The best organic scintillator has an efficiency of about 3.5%. For a more detailed discussion about organic scintillators take a look at the particle data group about scintillators and their references [2].

Calibration

Before using the scintillators we need to find out what the High Voltage (HV) is that maximizes the coincidence rate between the signals from PMT1,2 and 3 but is not too high in order not to have too much noise and random coincidences. Therefore we put the three scintillators on top of each other and look at the number of coincidences between PMT1, 2 and 3. We keep the voltage of PMT1 and 2 fixed at 2 kV and raise the voltage of PMT 3 in order to optimize the number of coincidence signals between PMT1, 2 and 3. The results are given in table 5.1.

As we see from table 5.1, the plateau lies at approximately 1.85 and 1.90 kV. Next, we set the voltages of PMT3 and PMT1 at respectively 1.90 kV and 2.00 kV and continue doing the same procedure described above but now with PMT2, counting the number of coincidence signals of PMT1 and 3 up to 1000. The plateau of PMT2 was found at 1.75 kV and 1.80 kV for PMT1. Table 5.2 gives the final operation voltages for the three PMTs.

Voltage on PMT3 (kV)	Coincidence between PMT	# of readings	Coincidence between PMT	# of readings
1.65	1 & 2	1000	1 & 2 & 3	74
1.70	1 & 2	1000	1 & 2 & 3	156
1.75	1 & 2	1000	1 & 2 & 3	240
1.80	1 & 2	1000	1 & 2 & 3	310
1.85	1 & 2	1000	1 & 2 & 3	374
1.90	1 & 2	1000	1 & 2 & 3	385
1.95	1 & 2	1000	1 & 2 & 3	398
2.00	1 & 2	1000	1 & 2 & 3	397

Table 5.1: Results of the calibration procedure.

	Voltage (kV)
PMT1	1.90
PMT2	1.75
PMT3	1.80

Table 5.2: PMT operation voltages.

5.2.2 Photomultiplier tubes

In the setup we are working with four photomultipliers, three connected to the scintillation counters (PMT1, 2 and 3) and one main PMT for collecting the Cherenkov radiation reflected by the mirror.

A photomultiplier converts light into an electric signal. Figure 5.3 shows the essential elements. The two phenomena fundamental to the operation of a PMT are *photoemission* and *secondary emission*. When a photon enters the PMT window it will transfer all its energy to bounded electrons of the photocathode material giving a fraction of them enough energy to escape. The free photoelectrons (*p.e.*) are then focussed and accelerated on to the first dynode where they cause secondary emission. Suppose n_c *p.e.* are focussed to the first dynode and the gain of the dynode is g_1 . Then the number of resulting electrons falling on the second dynode is $n_c g_1$. This multiplication process repeats itself at all succeeding dynodes. Finally when n_a is the number of *p.e.* collected by the anode, the current amplification A of a ten-stage multiplier is $A = \frac{n_a}{n_k} = \prod_{i=1}^{10} g_i$. In our case the amplification is about $6.5 \cdot 10^5$.

An important parameter relevant to the efficiency of our detector is, of course, the quantum efficiency $QE(\lambda)$. It is the ratio $QE(\lambda) = \frac{n_c}{n_\gamma}$ of the number of *p.e.* emitted, n_c , to the number of incident photons, n_γ . The absolute responsivity S_k spectrum of our PMT has a maximum at 420nm with $S_k = 90 \text{ mAW}^{-1}$. The responsivity and the quantum efficiency are related by the expression

$$QE(\lambda) = 1.24 \frac{S_k(\lambda)}{\lambda} \quad (S_k \text{ expressed in mAW}^{-1} \text{ and } \lambda \text{ in nm})$$

From this we can easily calculate that the upper limit of the quantum efficiency $QE(\lambda)_{max}$ is approximately $QE(\lambda)_{max} = 0.27$.

Because the signals from the Cherenkov radiation are very weak, we need to work with a PMT that has a very low noise. One important effect that can degrade the PMT's performance is known as dark current. The main causes of dark current noise are: (1) thermionic

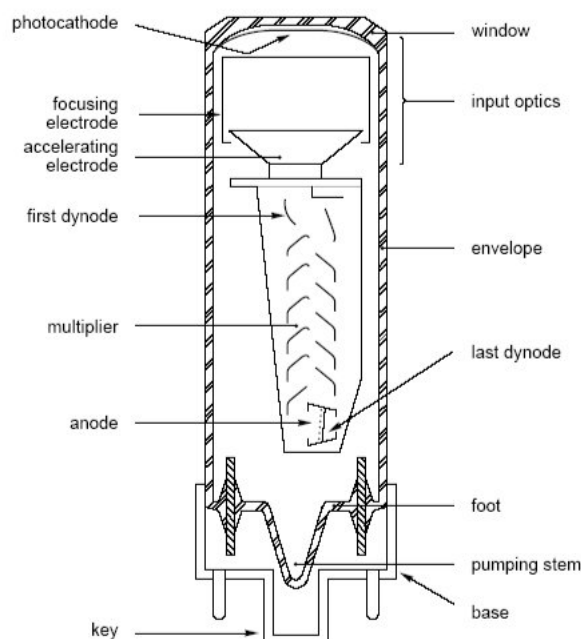


Figure 5.3: Photomultiplier tube diagram

emission, (2) leakage currents and (3) background radiation. At normal temperatures, thermal emission is dominant.

We have chosen to work with a low noise PMT. The photocathodes inside this PMT are made from a bi-alkali (SbKCs) material. At operating temperature of 10°C the number of dark pulses per second is 70 compared to tri-alkali (SbNa_2KCs) cathodes with a rate of about 1000 s^{-1} . Furthermore it is important to take into account that the time required for the dark current to settle down after switching on the PMT may delay the measurements for half an hour or more.

The PMT window is made from borosilicate glass which is transparent in the UV range of the spectrum. Contrary to fused silicate glass windows for example, this material has no Cherenkov-effect contribution to the dark current.

The dynodes inside our PMT are linearly focused. This reduces the variation in transit times between the 10 stages and makes a very fast response possible. Linear focused tubes, in which the electron impact areas on the dynodes are small, are most sensitive to magnetic effects. A magnetic flux density of $\sim 10\text{mT}$ could reduce the gain by 50%. To prevent such disturbances our tube is surrounded by a mu-metal shield.

5.2.3 The mirror

Producing the mirror

The making of the mirror has been a creative process. The workshop is able to make a lot of things, but it would take too much time to make a parabolic mirror out of wood or plastic. Because of that we have chosen to buy a satellite dish of which we removed the paint by hand. After this the dish has been cut in the right dimensions and chromed in a bath. The reflection of chrome is 65% at 450 nm which is in the middle of the range of our PMT (which

is [300,600]nm). The dimensions of the mirror are 36.2 cm by 25.7 cm. The depth at the center, compared to the outer borders is 1.4 cm.

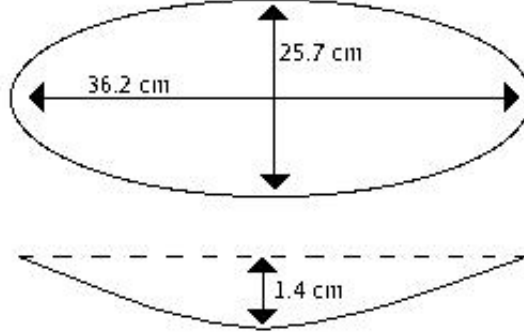


Figure 5.4: Geometry of the mirror.

5.2.4 The window

The opening within the flange, (8) in fig. 5.1, is closed with a borosilicate-glass window (4) in front of the main PMT. One of the main advantages of this glass, on top of the fact that it is UV transparent, is that it is far stronger than "soft" glass. Because the boron oxide particles inside the material are so small, the silicate is held together more closely resulting in a much stronger glass. The thickness of the window we use is 25mm and the diameter 178mm, enough to resist pressures up to 40 atm. The transmittance curve $T_{win}(\lambda)$ for a window with a thickness of 3 mm is shown in fig. 5.5, which gives us $\langle T_{win}(\lambda) \rangle_{3mm} \approx 0.88$. The curve from our window with a thickness of 25mm is just a power of this one². From the spectrum we can conclude that the transmittivity $T_{win}(\lambda)$ within the accessible PMT range [300,600]nm is approximately $\langle T_{win}(\lambda) \rangle = 0.55$.

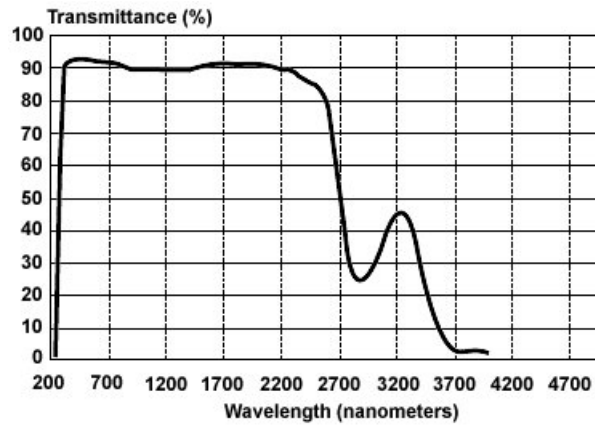


Figure 5.5: Window transmittance.

²The intensity drops as $I_0(d, \lambda) = e^{-\frac{d}{x_0(\lambda)}}$ with d the window thickness. Then $I_0(25, \lambda) = e^{-\frac{25}{x_0(\lambda)}} = (e^{-\frac{3}{x_0(\lambda)}})^{\frac{25}{3}} = (0.88)^{\frac{25}{3}} = 0.55$.

5.3 Estimated detector response

We are now able to give an estimation on the collected number of *p.e.*, assuming the photon yield N calculated in chapter 4. Fig. 5.6 shows three of the relevant parameters from eq. 5.3 as functions of the wavelength.

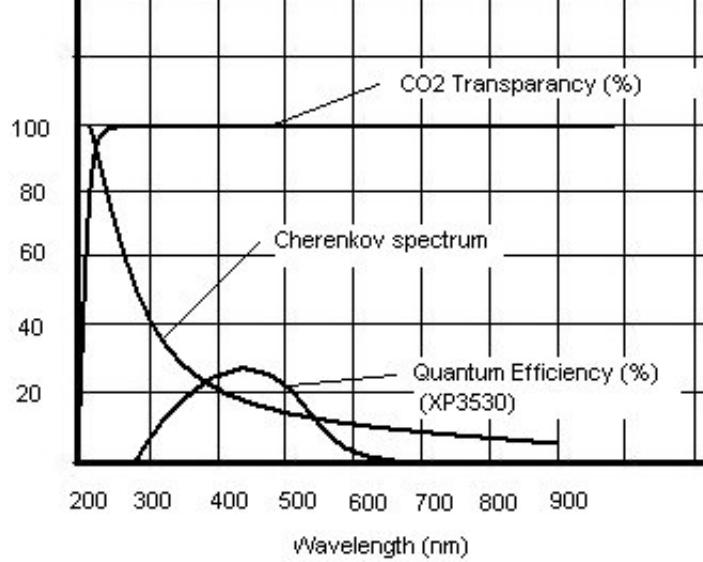


Figure 5.6: CO₂ transparency $T(\lambda)$, Cherenkov radiation distribution (in arbitrary units) and quantum efficiency curves as functions of the wavelength λ .

From fig. 5.6 we see that the opaqueness of CO₂ decreases rapidly after 200nm and disappears completely over the PMT-range [300,600]nm. The relevant parameters are given in table 5.3.

$QE(\lambda)_{max}$	$\langle T_{rad}(\lambda) \rangle$	$\langle T_{win}(\lambda) \rangle$	$R(\lambda)_{max}$	$\epsilon_{det}(\lambda)_{max}$
0.27	1.00	0.55	0.67	0.59

Table 5.3: Setup reduction parameters.

Then the maximum number of p.e. collected by the main PMT, given by eq. 5.4 will be

$$\begin{aligned}
 N_{p.e.} &= QE(\lambda)_{max} \epsilon_{det}(\lambda)_{max} N \\
 &= 12.44
 \end{aligned} \tag{5.5}$$

This corresponds to a typical quality factor N_0 (eq. 5.3) of about 76cm⁻¹. Practical counters, utilizing a variety of different photodetectors, have values between about 30 and 180cm⁻¹. The real value of N_0 must be lower than 76cm⁻¹, because we did not include the geometrical photon collection efficiency ϵ_{coll} in our calculations.

Chapter 6

Measurements and Analysis

The gas Cherenkov detector has finally been assembled and ready to take measurements in January 2005. During the following two months a total of eight data sets were taken with the detector, each one with a different gas composition and refractive index. The run time for each data set was between 17-50 hours as we wanted to have large number of events for the data analysis.

6.1 Event display

For each trigger, the output of the two data channels is displayed in real time on the computer screen. Later we are able to display the events again using the output text file. For example, in fig. 6.1 you can see a single event displayed. The blue (darker) curve gives the scintillators' output channel, the red (lighter) curve gives the Cherenkov counter channel. In this case the trigger (scintillator signal) is seen, but there is no signal from the Cherenkov counter. In fig. 6.2 an event is shown containing a signal from the Cherenkov counter - this is the small dip at 50nsec before the trigger. It is clear that the coincidence unit signal is much stronger than the Cherenkov signal.

6.2 Presentation of the measurements

During the months January - February 2005 a total of 8 data sets have been taken with the detector. Table 6.1 on page 52 gives the information about the different data sets. In the literature we found these values for n , the refractive index. For $P = 1$ atm and 0°C conditions: $n(\text{CO}_2) = 1.000410$, $n(\text{air}) = 1.000293$. For $P = 1$ atm and 25°C : $n(\text{CO}_2) = 1.000500$ and for $P = 1$ atm and 20°C : $n(\text{air}) = 1.000273$. We estimated the temperature at the hall where the Cherenkov counter was taking measurements at $10^\circ \pm 3^\circ\text{C}$, and so we calculated the n_0 that corresponds to these temperatures:

$$(n_0(\text{CO}_2) - 1) \cdot 10^6 = 446 \pm 10.8 \quad , \quad (n_0(\text{air}) - 1) \cdot 10^6 = 283 \pm 3$$

For the first data set the pipe has been filled with CO_2 gas up to a pressure of $P = 1.7$ atm on top of the air at $P = 1$ atm that was in the pipe. After the measurement, the safety valve on top of the pipe has been opened so that most of the air could escape out of it. We then closed the valve and let more CO_2 gas flow into the pipe, so the second measurement was done with $P(\text{air}) = 0.37$ atm and $P(\text{CO}_2) = 2.33$ atm. We repeated the flushing procedure after the second and the third data sets, so as from the forth data set the air pressure in the

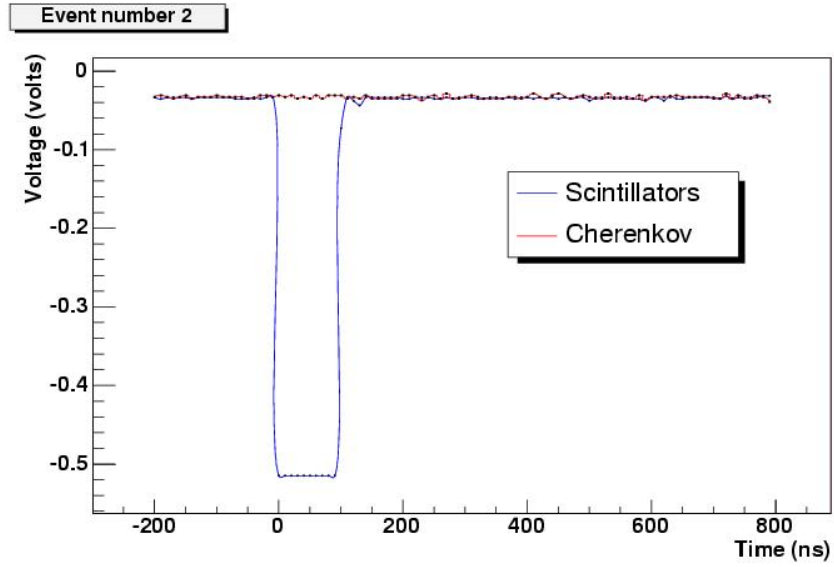


Figure 6.1: Single event display - trigger, no signal from the Cherenkov counter

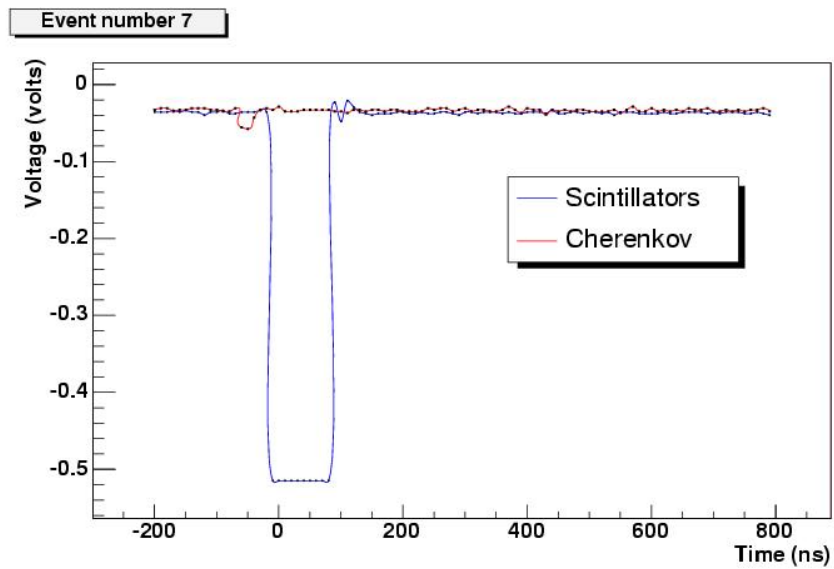


Figure 6.2: Single event display - trigger and observable signal from the Cherenkov counter

detector was minimal, approximately $P(air) = 0.06$ atm. For each data set we calculated the refractive index of the specific gas mixture and its error using the relations:

$$n_{tot} - 1 = (n_0(CO_2) - 1) \cdot P(CO_2) + (n_0(air) - 1) \cdot P(air) \quad (6.1)$$

$$P_{tot} = P(CO_2) + P(air) \quad (6.2)$$

We assume $\delta P_{tot} = 0.05$ atm from the accuracy of the pressure meter, so we have

$$\delta P(air) = \frac{P(air)}{P_{tot}} \cdot 0.05 \quad , \quad \delta P(CO_2) = \frac{P(CO_2)}{P_{tot}} \cdot 0.05 \quad (6.3)$$

We define the useful value $\tilde{n} \equiv (n_{tot} - 1) \cdot 10^6$, so we get the error to be

$$\delta \tilde{n} = \sqrt{(\delta P(CO_2) \cdot 446)^2 + (10.8 \cdot P(CO_2))^2 + (\delta P(air) \cdot 283)^2 + (3 \cdot P(air))^2} \quad (6.4)$$

The trigger rate is calculated by dividing the total number of triggers measured by the time length of the measurement. The trigger rate should be approximately constant at all runs, taking into account that the number of cosmic ray muons hitting the scintillators has statistical fluctuations, and some day and night effect should be expected as well. If we look at the trigger rate values, the calculated average is $\bar{N}_{trig} = 303.3$ trigger/hour. When we measure the trigger rate we can expect a spread in the values according to $303.3 \pm \frac{\sqrt{303.3}}{\sqrt{8}} = 303.3 \pm 6.15$. The 8 measured values are within 1.64σ distance from the mean, so we can say that it is likely that these measurements represent the same value.

run #	date (started)	trigger rate (1/hr)	total # of triggers	total pressure ±error (atm)	refractive index ($n - 1$) * 10^6 ±error	comment
1	26-01-2005	295.4	5012	2.7±0.05	1041.2±23.89	pressure reduced to 2.4 atm overnight
2	27-01-2005	304.3	7862	2.7±0.05	1143.89±31.76	measurement started with 2.7 atm pressure. stabilized at 2.65 atm
3	28-01-2005	302.1	15001	2.2±0.05	958.38±30.53	pressure fell back during the night to 2.0 atm
4	03-02-2005	298.8	7269	1±0.05	436.22±23.31	
5	04-02-2005	307.9	15001	1.4±0.05	614.62±25.8	
6	08-02-2005	300	13747	1.8±0.05	793.02±28.6	
7	10-02-2005	304.6	8000	2.2±0.05	971.42±31.7	pressure dropped to 2.1 atm overnight, put back to 2.2 atm next day and fell back again to 2.1
8	11-02-2005	313.4	15001	2.6±0.05	1149.82±35.03	

Table 6.1: Table of the measurement conditions. The date stated is the date on which the measurement started. The trigger rate is calculated by dividing the total number of triggers by the time length of the measurement. It should be approximately constant at all runs. The total pressure is the sum $P(\text{CO}_2) + P(\text{air})$, at runs 1-3 the air pressure is non-negligible. The total pressure error is taken from the pressure meter accuracy.

6.3 Data analysis

The first thing we want is to select from the data sets the events that have a signal from the Cherenkov counter in them. Once this selection has been done, several interesting values such as the signal rate, average of the signal maximum height and signal to trigger ratio are calculated. In order to optimize the data analysis and to be able to cross check our results we have split into two teams, one team using the ROOT framework to perform the analysis while the other team has worked with PAW.

6.3.1 Data analysis using PAW

First, we make a histogram of the mean pulse height of each data set. We find out that the Cherenkov signal is between the 12th and the 24th bin. Then we add up all counts of those bins and subtract half the sum of the counts which we found in the bins 1 to 12 and 24 to 36. This gives us a normalised spectrum of mean pulse heights as can be seen in fig. 6.3 on page 53. The spectrum is of course dominated by the data which do not contain any events. The rightmost very large peak contains data without a Cherenkov signal. If we would be able to subtract this peak, which is actually a gaussian, we should be left with several smaller gaussians, where each gaussian represents Cherenkov events with a similar number of photons reaching the main PMT. It is therefore important to remove the noise peak without losing much of the events data.

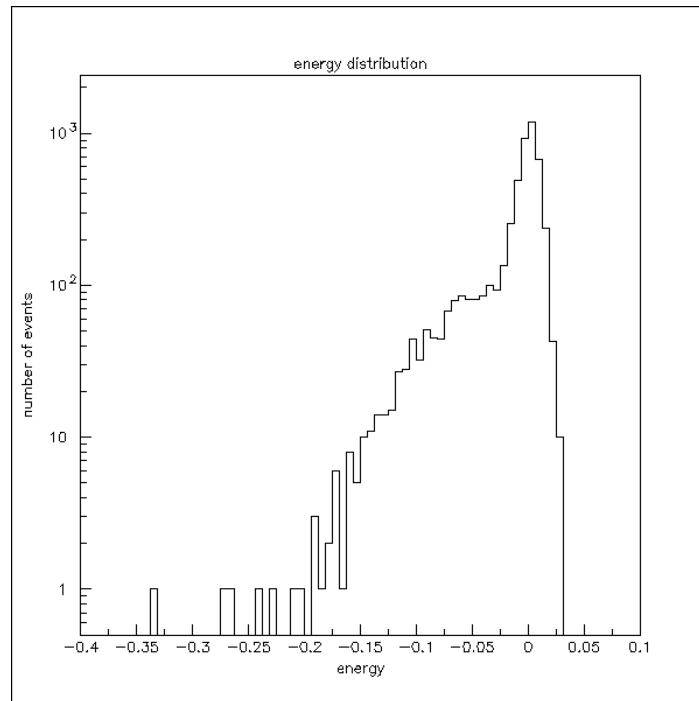


Figure 6.3: **PAW**: Histogram of the first data set. The gaussian (rightmost) noise peak around 0 is very clear and should be removed to find anything next to it.

Sigma clipping

To remove the noise peak, some options have been tried. First we took the statistical approach. This means that we wrote a program which rejects any pulse of which the maximal deviation from the mean pulse value is separated more than three standard deviations (3σ) from that mean. This approach should discriminate between noise and data with an accuracy of 99.9% (which means that any point within those error bars is 99.9% sure to be a data point). To see how sensitive the data are to such a cut we also plotted a graph of which the rejection factor has been set to 6σ (fig. 6.4 on page 54). In the figures you can see how the difference between the 3 and 6σ cuts affects the rightmost data points. (You observe that less events are left after the 6σ cut. This is of course what one would expect, as when using a 6σ cut it is more likely that some real events would be rejected together with the noise).

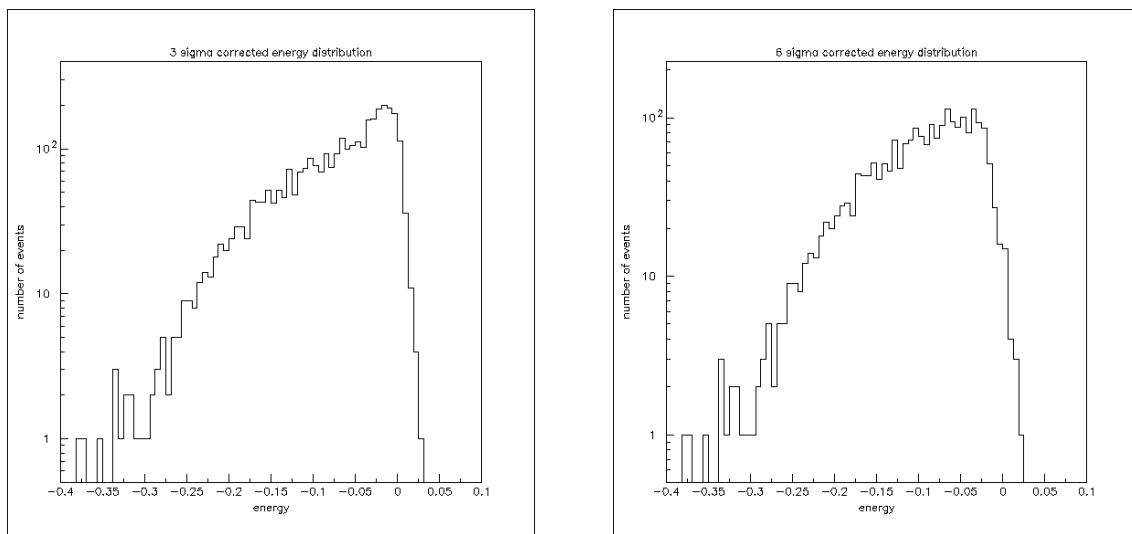


Figure 6.4: Graphs of the statistical cut method. For the **Left** graph, a cut of 3σ has been applied. The **Right** one represents the 6σ cut data. One can see that there is some effect of the cut on the number of data points, so we should not exaggerate with this sigma level

Reconstructing a noise peak

As another method to subtract the noise we have reconstructed a noise peak in a similar way we constructed the data set. To do this we have used the procedure described above for the creation of the data histogram, but then started from the last bin backwards. So we added up the counts from bins 100 to 88 and from bins 76 to 64 and subtracted half this number from the sum of the bins 65 to 87. This created a peak which we normalised, based on the maxima of the data noise peak and the just created one. Then we subtracted the normalised noise peak from the data set. A typical result can be seen on fig. 6.5 on page 55. As one can directly see from the figure, this method is not totally flawless. Because the noise is a gaussian centered around 0 and because in principle all data yield a negative number, the positive values of the data should be noise.

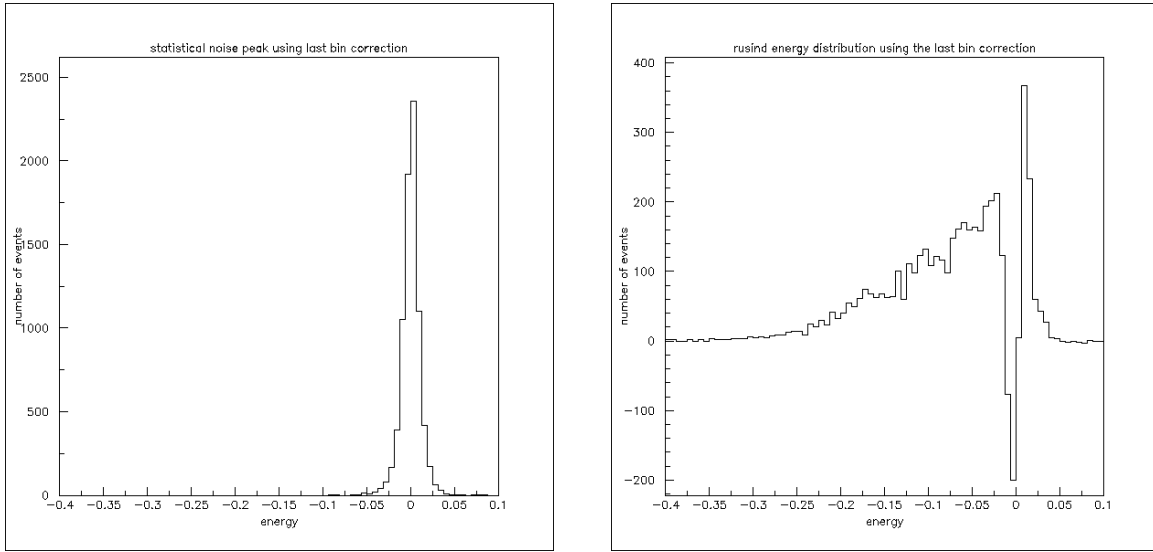


Figure 6.5: **Left:** The noise peak created by counting the last bins of the data set. **Right:** The data with this noise peak normalised and subtracted.

Mirroring noise over data

The last try we did to get rid of the noise was to mirror the positive part of the histogram and to subtract the peak we created this way from the data. The result of this work is shown in fig. 6.6 on page 55 and is similar to that of fig. 6.5. Another idea, which we did not manage

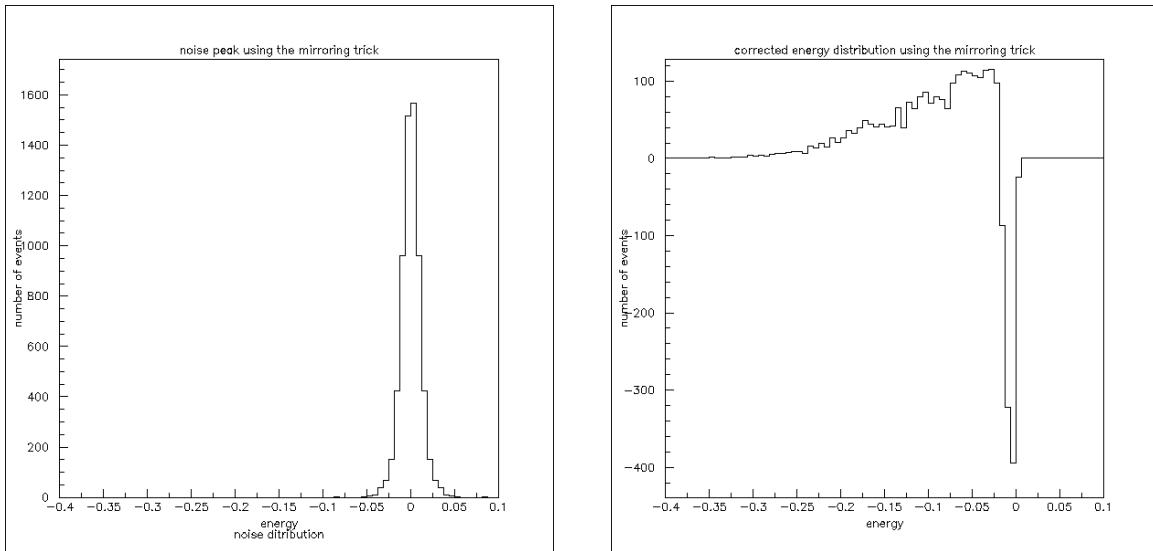


Figure 6.6: **Left:** The noise peak created by mirroring the positive values of the histogram. **Right:** The data with this noise peak subtracted.

to work out in detail because of lack of time was to take one of the two 'artificial' peaks and fit a gaussian to them. Then a gaussian with the same Full Width at Half Maximum should be fitted to the noise peak of the data. A quick fit however gave the same results as both artificial peaks gave anyway.

For the further processing of the data we have decided that we should use a 3σ clipping. Sigma clipping is the method which leaves us with the best spectrum. We have chosen 3σ because we think that this should leave as much real data as possible without contaminating it with too much noise.

6.3.2 Data analysis using ROOT

Similar to the PAW analysis we use a 3σ clipping to select the Cherenkov events. We notice that the Cherenkov signal always appears between -80nsec to 40nsec so we integrate over this range. We calculate the average noise level using the ranges -200nsec to -80nsec and 400nsec to 520nsec, thereby we choose to take readings from times long after the trigger has gone back up since the trigger has some fluctuations due to reflections when it goes back up, as seen in fig. 6.2 on page 50, and this might induce a signal in the other channel. Then we correct the signal level to signal on top of the noise level. We then plot the entire Cherenkov signal level on top of the noise level for all the triggers taken in the Run. Fig. 6.7 shows this plot for run 8. The prominent peak on the right has in it triggers that do not have Cherenkov events (so noise level only), the more spread out data on the left represents signals of Cherenkov events. In order to select the Cherenkov events from this distribution we calculate the average noise level and the standard deviation. For each measurement we search for the minimum signal value between -80nsec to 40nsec. If the minimum value is less than the average noise level subtracted by 3 times its standard deviation (σ) then this measurement is declared a Cherenkov event. Fig. 6.8 on page 58 contains the entire signal level (same value as in 6.7) but only for the selected events. Fig. 6.9 on page 58 shows the distribution of the minimum signal level value of the selected Cherenkov events.

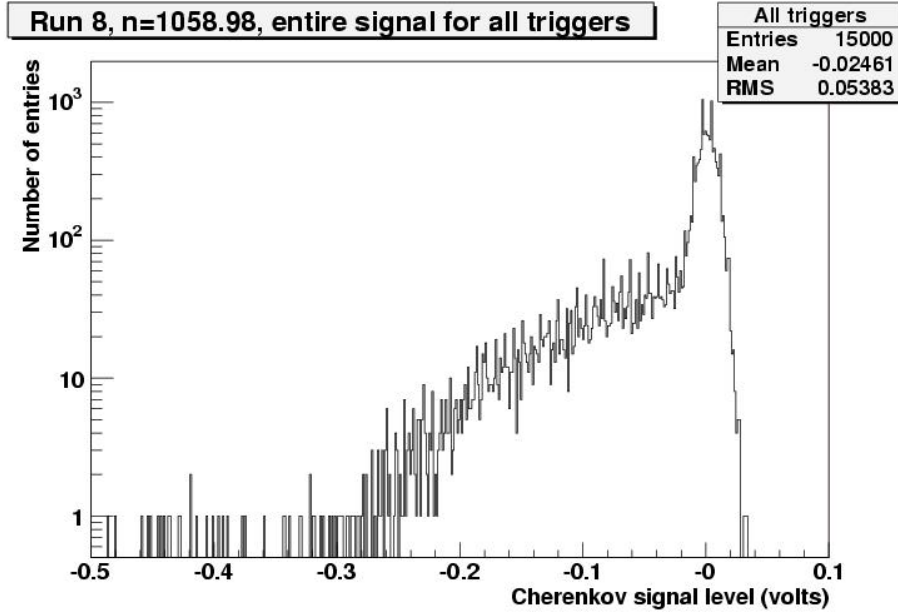


Figure 6.7: Run 8, the entire signal level from the Cherenkov counter for all the triggers that were taken

The number of events obtained from this selection procedure is similar to that obtained with the PAW analysis for most runs. After the selection certain values were calculated from the Cherenkov events of each data set. These values are reported in the next chapter: Results and Discussion.

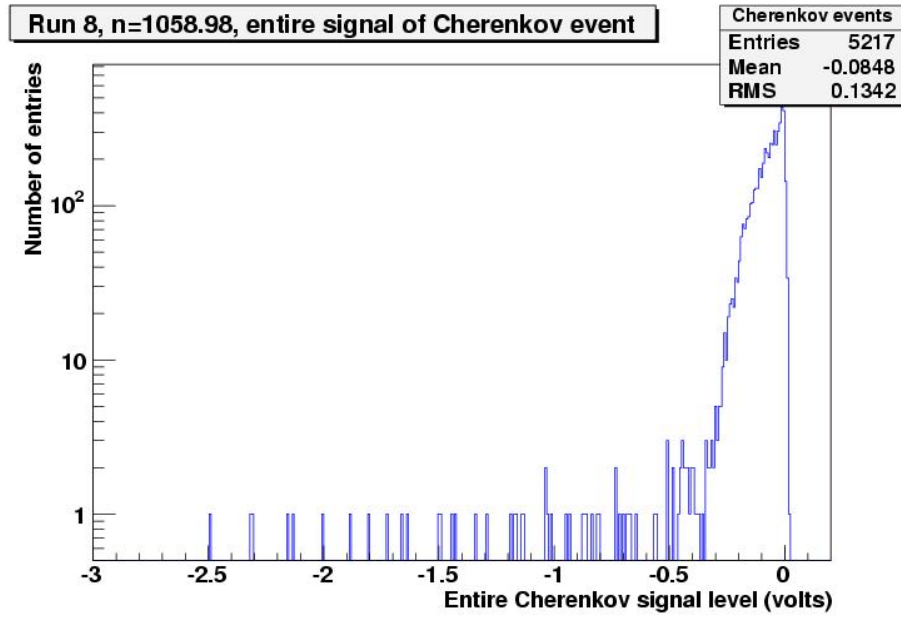


Figure 6.8: Run 8, selected Cherenkov events with 3σ selection, the entire signal level from the Cherenkov counter

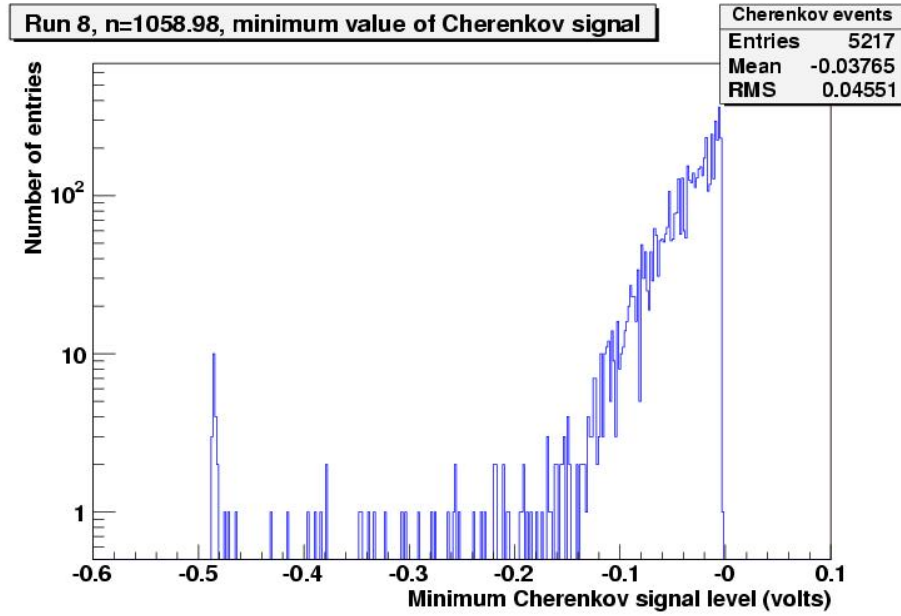


Figure 6.9: Run 8, selected Cherenkov events with 3σ selection, the minimum value of the Cherenkov signal

Chapter 7

Results and Discussion

In this chapter we present the results from our experiment. We start by reporting all the obtained values in results tables and afterwards we present some of the more interesting results in graphs. Later we show a comparison between the experimental results and the simulation predictions. Finally we draw conclusions on the project and make suggestions for the future work with our Cherenkov detector, which will hopefully help to achieve better results with it.

7.1 Results tables

Table 7.1 on page 65 and table 7.2 on page 66 contain the results from the PAW and ROOT data analysis. From the statistics in the two tables we see that the PAW and ROOT analyses got similar figures concerning number of Cherenkov events in each run and the mean of the minimum signal value. The ROOT analysis reports a larger number of events than the PAW analysis for all runs, but the difference between the two is always smaller than 5.8%, so not very big. Generally we observe that the mean of the minimum signal level decreases (negative signal) as the refractive index increases. We see that the trigger level is approximately constant and that the Cherenkov event rate increases with the refractive index. The Cherenkov event to trigger ratio behaves the same way of course, as it is the Cherenkov event rate divided by (approximately) a constant.

7.2 Graphic presentation of results

We now present graphically the interesting results obtained from the analysis. Fig. 7.1 on page 60 shows the Cherenkov to trigger rate ratio vs. the effective refractive index for the eight data sets. Fig. 7.2 on page 61 shows the Cherenkov event rate vs. the refractive index and fig. 7.3 on page 61 shows the minimum value of the Cherenkov signal vs. the effective refractive index.

Looking at fig. 7.1 we see that as expected, the Cherenkov to trigger ratio increases with the refractive index. But the eight data sets do not seem to agree completely, we cannot reconstruct a curve that defines the ratio to refractive index relation that agrees with all the data points. Naturally this is the case in fig. 7.2 as well. In fig. 7.3 we see that the minimum signal value decreases with increasing refractive index, but similar to the previous plots, the data points are not completely consistent.

We observed that in run1 and in run2 the measured Cherenkov to trigger ratio is smaller than

what it is expected to be according to all the other measurements. The obvious difference between runs 1 and 2 to the later measurements is that in the first three the measurements were taken with a non-negligible amount of air in the detector. Therefore we searched and found that both Nitrogen and Oxygen, which are the building blocks of air, have absorption lines in the range of 300-600nm, which is the working range of the Cherenkov PMT [9] [10]. We then conclude that in these first 2 runs we have less Cherenkov events than what we expect due to some absorption of photons by the air molecules, and this is why the data points are not consistent with the rest of the measurements.

Looking at the minimum signal value plot we observe that runs 1 and 3 are not consistent with the other measurements. Runs 1 and 3 give higher value than expected, which means less photons than expected arriving to the PMT per Cherenkov event.

This observation of less strong signals agrees with the previous one if our understanding of the reason for it is correct. However, we cannot explain why in the Cherenkov rate plots it is run 1 and run 2 that are off while in the minimum signal value it is run 1 and run 3 that are off.

Unfortunately, due to the low number of measurements taken, and due to the apparent low number of detected Cherenkov events in the first three measurements (lower number than expected due to the air-CO₂ gas mixture), we do not try to fit the measurements into curves and compare the fit parameters to theoretical calculated values, which in most cases are not at hand anyway. We shall compare our results to the simulation predictions.

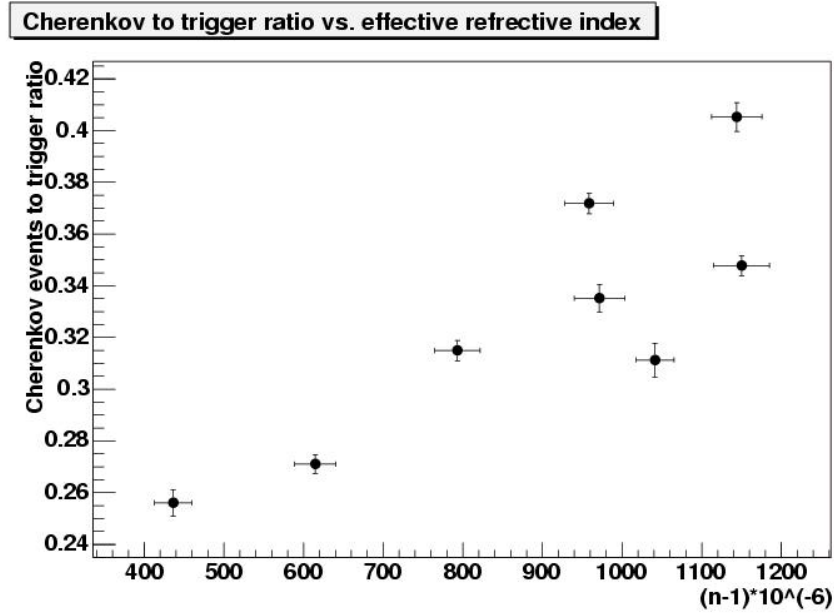


Figure 7.1: Cherenkov to trigger rate ratio vs. the effective refractive index for the 8 data sets.

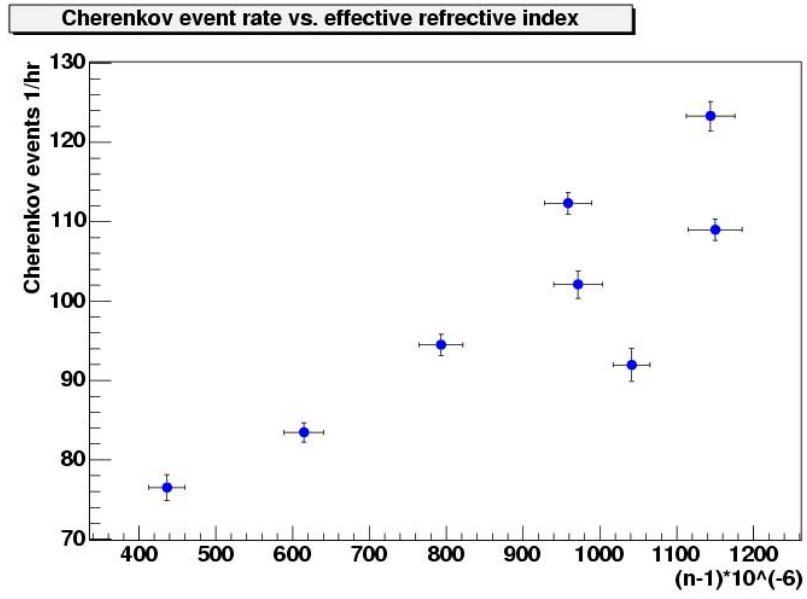


Figure 7.2: Cherenkov event rate vs. the effective refractive index for the 8 data sets.

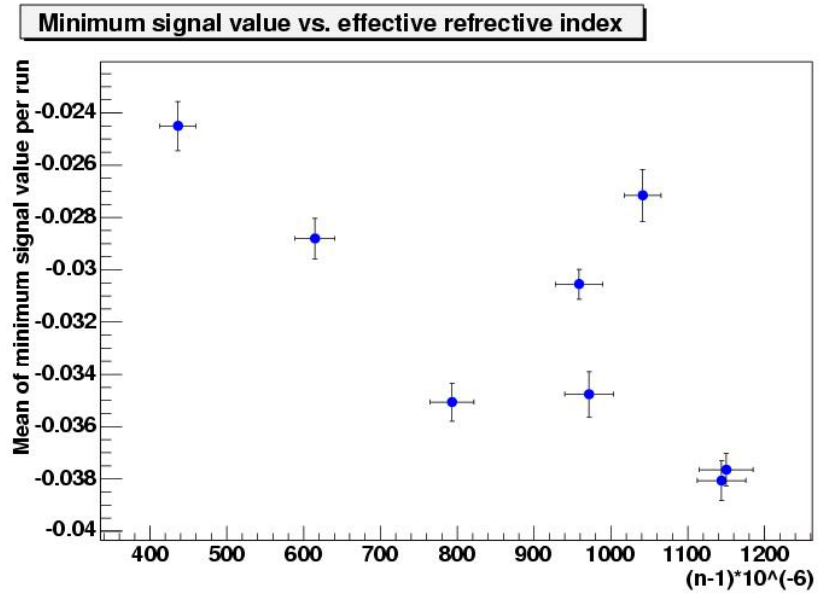


Figure 7.3: Mean Cherenkov minimum value vs. the effective refractive index for the 8 data sets.

7.3 Comparison with simulation predictions

After recording the data sets with the detector we have run the simulation program with the exact pressures of the data sets so we can compare between the two. The full simulation output information is reported in table 4.2 on page 36. Comparison between the experimental data and the values obtained from the simulation is shown in table 7.3 on page 67.

We notice a few interesting things by looking at the table:

Trigger rate

Firstly, the simulated trigger rate is completely constant, as expected from a computer program that was designed that way. The error for this value is calculated in the last part of section 4.4. We notice the difference between the simulated trigger rate, 372.36 (1/hr), and the average of the experimental trigger rate, 303 (1/hr). The experimental trigger rate is smaller by $\sim 19\%$ from the simulated value (however, this difference is only 1.25 times the error of the simulated trigger, as the error is estimated at 15%). There could be several reasons for that. The most obvious one is that our trigger setup, which includes three scintillators, three PMTs and a coincidence unit, is not 100% efficient, but we also cannot estimate its true efficiency precisely. This is not implemented in the simulated trigger rate but, using an estimation of the efficiency, in its error. This is also the reason why the error is relatively large.

And so we conclude that for the comparison to come, we should use the simulated trigger and event rates subtracted by their calculated errors, in order to include the real detector efficiency. And still, we should expect to find a difference of at least 4% between the “corrected” simulated Cherenkov event rate and the measured one. This however should not have an effect on the event to trigger ratio.

Cherenkov event rate

Secondly, we look at the difference between the experimental event rate and the simulated one. Here the difference is much bigger. To simplify things we will look only on runs 4 to 8, as we have already seen before that runs 1 to 3 do not give us the statistics which are consistent with the later runs. Starting from run 4 with low refractive index, in which case the experimental value is 45% lower than the simulated one, and increasing together with the refractive index, in run 8 the difference is more than 51%. It looks as if the difference in the event rates is more than twice as big as the difference in the trigger rates. However, the simulated event rate value has a rather large error, as seen and explained in the last part of section 4.4. If we look at the event rate value subtracted by the estimated error, we get a difference of only 22% to 29% for runs 4 to 8. If we continue and subtract the 19% which is the correction “inherited” from the trigger rate we are left with a difference of 3% to 10% between the simulated and experimental values.

Cherenkov event to trigger ratio

Next we look at the difference between the experimental Cherenkov event to trigger ratio and the simulated value. Here the difference goes from 30% for a low refractive index run and up

to 42% for high refractive index run. We believe that the large difference here is due to the true efficiency of the Cherenkov detector itself. Some of the elements of the detector and their effect of lowering down the efficiency of the detector were not implemented in the simulation: the reflectivity in the mirror and the deviations from a perfect oval shape of the mirror. It is also probable that other elements determining the efficiency of the detector which were implemented in the simulation (like the transmittivity of the window, the quantum efficiency of the main PMT and so on) decrease the detector's efficiency more than what was expected.

7.4 Conclusions

- While working on the NIKHEF project we have learned the theory of Cherenkov radiation and the technical aspects of how Cherenkov detectors work. We have had the experience of working with mechanical engineers and the mechanical workshop. Also we gained some experience working with PAW (using FORTRAN) and ROOT (using C++).
- We conclude that our detector design has been very successful as we have a fully working gas Cherenkov detector.
- Though we took measurements with the detector and analysed its data, we were not able to obtain the energy spectrum of the atmospheric muons. To achieve the energy spectrum many more data sets, and the ability to determine the number of photons reaching the PMT per event are necessary. As we believe that only very few photons reach the PMT for every event, it is doubtful even for a run with high refractive index if one can measure the energy spectrum.
- In our data analysis we did find for the Cherenkov event rate and the mean Cherenkov minimum signal value the general behaviour that was expected from the theory.
- Comparing the experimental values of the Cherenkov event rate, the trigger rate and the ratio between the two to the simulation predictions, we found that the experimental values are at most 2σ smaller than the simulation values. The largest difference between the two was found in the event rate parameter. Other parameters show better agreement between the experiment and the simulation. We conclude that, taking into account its error range, which mostly represent our lack of knowledge of the detectors true efficiency, the simulation programme describes the experiment well.

7.5 Suggestions for future work with the detector

- In the future we suggest to expel all the air from the pipe before starting to take measurements, as we have seen that the air in the pipe reduces the number of detected Cherenkov events.
- Using CO₂ gas as a radiator, we did not manage to reach higher pressures than 2.8atm since the gas condensated in the pipe at higher pressures. For future data taking with the detector it would be advisable to use a different gas, preferably one with higher refractive index than CO₂, such as Freon gas, but more importantly a gas that could be pumped up to higher pressures inside the pipe.

- The simulation program should be updated with the real detector efficiency which should be estimated from the already analysed data, so for future runs of the detector the simulation could give better predictions for the detected values.
- If more data sets with higher refractive index would be taken, one could fit a curve to the data points in fig. [7.2](#) and compare the fit parameters with the theoretical values.

run #	$(n - 1) * 10^6$	# triggers	# events (PAW)	#events (ROOT)	minimum signal value PAW	minimum signal value ROOT	rms in mean ROOT	error in mean ROOT
1	1041.2 \pm 23.89	5012	1532	1560	-.0275	-.0272	.0391	.0010
2	1143.89 \pm 31.76	7862	3155	3186	-.0384	-.0381	.0430	.0008
3	958.38 \pm 30.53	15000	5503	5577	-.0309	-.0306	.0426	.0006
4	436.22 \pm 23.31	7269	1754	1861	-.0257	-.0245	.0405	.0009
5	614.62 \pm 25.8	15000	3966	4065	-.0294	-.0288	.0491	.0008
6	793.02 \pm 28.6	13746	4251	4329	-.0356	-.0351	.0480	.0007
7	971.42 \pm 31.7	7999	2603	2681	-.0356	-.0348	.0450	.0009
8	1149.82 \pm 35.03	15000	5089	5217	-.0385	-.0377	.0455	.0006

Table 7.1: Results table. The number of Cherenkov events in the PAW and ROOT analysis are similar, the mean values of the minimum signal value in both cases are also similar. From the statistics given for the ROOT analysis we see that the minimum signal value is very much spreaded (also observed in figure 6.9), it is not constant in the events. This is due to the fact that different events have different number of photons reaching the PMT, thus creating different signal level for each event.

run #	$(n - 1) * 10^6$	trigger rate (1/hr)	event rate (1/hr)	events/triggers ratio	ratio error
1	1041.2 \pm 23.89	295.4180	91.9496	0.311252993	0.00654005
2	1143.89 \pm 31.76	304.2600	123.2980	0.405240397	0.005536822
3	958.38 \pm 30.53	302.1280	112.3310	0.3718	0.003946009
4	436.22 \pm 23.31	298.8040	76.4994	0.25601871	0.005118934
5	614.62 \pm 25.8	307.9210	83.4466	0.271	0.003629132
6	793.02 \pm 28.6	299.9820	94.4728	0.314927979	0.003961736
7	971.42 \pm 31.7	304.5600	102.0780	0.335166896	0.005277996
8	1149.82 \pm 35.03	313.3730	108.9910	0.3478	0.003888746

Table 7.2: Results table from the ROOT analysis. The trigger rate is approximately constant, the Cherenkov event rate rises with the refractive index and accordingly the Cherenkov event to trigger ratio. Results from the first 3 runs, which were made with an air-CO₂ gas mixture, are not consistent with runs 4 to 8. We believe that this is due to absorption lines existing in Nitrogen and Oxygen at the wavelengths range the PMT is working with, 300nm-600nm, and so the photons may be absorbed and the intensity of the signal is lower than expected.

run #	$(n - 1) * 10^6$	trigger rate (1/hr)	simulation trigger rate (1/hr)	event rate (1/hr)	simulation event rate (1/hr)	events/triggers ratio	simulation eve/trig ratio
1	1041.20±23.89	295.42	372.36±55.85	91.95	208.32±47.37	0.3112±0.0065	0.5595±0.1521
2	1143.89±31.76	304.26	372.36±55.85	123.30	218.28±49.64	0.4052±0.0055	0.5861±0.1594
3	958.38±30.53	302.13	372.36±55.85	112.33	203.08±46.18	0.3718±0.0039	0.5454±0.1485
4	436.22±23.31	298.80	372.36±55.85	76.50	138.84±31.54	0.2560±0.0051	0.3729±0.1014
5	614.62±25.8	307.92	372.36±55.85	83.45	162.74±36.98	0.2710±0.0036	0.4371±0.1189
6	793.02±28.6	299.98	372.36±55.85	94.47	188.27±42.80	0.3149±0.0037	0.5056±0.1376
7	971.42±31.7	304.56	372.36±55.85	102.08	208.04±47.30	0.3351±0.0053	0.5587±0.1520
8	1149.82±35.03	313.37	372.36±55.85	108.99	223.92±50.93	0.3478±0.0039	0.6013±0.1638

Table 7.3: Comparison between experimental data and simulation values.

Bibliography

- [1] *Particle Data Group*: July 2004 Particle Physics Booklet
CERN and LBNL (2004)
- [2] *S. Eidelman et al.*: Review of Particle Physics online (<http://pdg.lbl.gov/>)
CERN and LBNL (2004)
- [3] *A. W. Wolfendale*: Cosmic Rays at ground level
The Institute of Physics, London and Bristol (1973) *Particle Data Group*: July 2004
Particle Physics Booklet
Experimental Methods and Colliders / Particle detectors (Rev.)
- [4] *Energy determination in the Akeno Giant Air Shower Array experiment*: arXiv:astro-ph/0209422v3 Nov 2002
- [5] *V.P. Zrelov*: Cherenkov radiation in high-energy physics, Part 1
Moskou 1968
- [6] *H. Ulrich et al.*: Primary energy spectra of cosmic rays selected by mass groups in the knee region.
Proceedings of 27th ICRC, Hamburg (2001) 97
- [7] *The HEF4 project group*: The construction of a water Cherenkov detector
(<http://www.nikhef.nl/~mlimper/cerenkov/cerenkov.html>)
- [8] http://www.nikhef.nl/pub/departments/mt/projects/Cherenkov_2004/
- [9] <http://physics.nist.gov/PhysRefData/Handbook/Tables/nitrogentable2.htm>
- [10] <http://physics.nist.gov/PhysRefData/Handbook/Tables/oxygentable2.htm>